Appendix 6 - Characterization of sediment plumes behind mining vehicles in the NORI area

iSeaMC GmbH • Campus Ring 1 • 28759 Bremen • www.iseamc.com

Characterization of sediment plumes behind mining vehicles in the NORI area (laboratory analyses)

Authors: Benjamin Gillard and Laurenz Thomsen

iSeaMC@OceanLab

Bremen, 11.11-2020
5rt draft

CEO:
Dr. Olaf Pfannkuche: o.pfannkuche@iseamc.com

VAT Reg.No.: DE 306560014
Bremen HRB 31356 HB

Summary

- Sediments from the Nori-D site for aggregation experiments and Type 1 nodules for experiments on blanketing were delivered by DG, AllSeas and BF. A test section for a seawater flume was prepared for the nodules using original sediments.
- Two flow conditions were simulated: 3.5-4 cm/s average flow velocity at the mining site (resembling a shear rate of ≈ 0.1 G), and 15 cm/s (flow velocity of an eddy passing through the mining site under 1G).

Results

- Plume dispersal in the near-field area with concentrations of 1 – 10 g/l dw (≈ 40 g/l sediment wet weight) of sediments (0-15 cm) under elevated (1G, 15 cm/s) and normal (0.1 G, ≈ 4 cm/s) turbulence results in rapid aggregation of deep sea sediments after they passed through the high-shear collector pump .
- As expected by theoretical and empirical studies on aggregation, the process starts immediately. Under both concentrations, larger particles with median sizes (d_{50}) of ≈ 700 µm (0.1G) and ≈ 2000 µm (1G) are formed within the first 30 minutes while particle fallout takes place simultaneously.
- For both scenarios, a rapid export phase of the aggregates lasts for around 120 min and particle concentrations drop well below 10 % of the original concentration.
- Constant release of plumes particles will extend that export phase over hours to days, while the "Core aggregation" phase towards large aggregates remains fast but will also constantly take place.
- Settling velocities of individual aggregates in stagnant waters of a settling column under these elevated plume concentrations varied between 62 and 705 m/day. **These results can be used for particles settling at a midwater point , in the water column (1000-4000 m)or well above a fluid mud layer in the benthic boundary layer.**

For the fluid mud layer which develops behind the collector we also applied another approach to better understand the behavior of concentrated plume injections ≥ 1g/L to determine effective settling velocities under hindered settling (see below). For that we used the data from an Aqualogger turbidity meter, which automatically adapts to increasing particle concentrations. The calculated settling velocities were much lower for a floc population, which was exposed to both, hindered settling and turbulence. This behavior can be expected in highly concentrated plumes.

- Under averaged settling velocities of 0.013 cm/s for floc populations developing under plume concentrations of 10 g/L, these particles can be transported over tens of kilometers under the conditions of hindered settling.
- During mining operations with constant plume release a fluid mud layer is formed from "hindered settling" which consists of un-consolidated loose aggregates which should easily form a gravity flow. This fluid mud layer is compacted and consolidated over time but remains unstable and loose as long as particles settle into it.
- Once the plume release is stopped, the fluid mud layer is compacted and decreases its thickness within hours.
- Type 1 nodules are easily blanketed by this consolidated mud layer and in the far field area with particle concentrations < 1500g/L a linear relationship between blanketing thickness, sediment load and particle concentration was determined which allows DG to estimate blanketing under different scenarios of plume concentrations and duration. For the near field area a scenario was developed for > 10/L deposition.
- For the near filed scenario with particle concentrations between 1 and > 10 g/l the accumulating blanketing layer will be further compacted and consolidated by its increasing mass.
- Under higher plume concentrations of 10 g/l fine particles not scavenged by the aggregation process remain in the water column for days. When they reach the seafloor without being scavenged by larger aggregates, they form a very fine powder-like cohesive top-layer of the blanketing.

- Once Type 1 nodules are completely blanketed, this layer prevents resuspension up to flow velocities of 15 cm/s and creates a new sediment surface at the exploration site.

I. Overview

The dispersal of a sediment plume during mining operations poses the biggest impact for the deep sea environment. A reliable forecast of the fallout areas of the generated plume is important and reliable data on the behavior of plume particles are therefore essential. Following the discussion with Deep Green we hereby report data and recommendations from laboratory studies with original sediments from the NORI exploration site.

Depending on the hydrodynamic conditions and aggregation potential of the sediment plume, aggregates of different particle sizes will settle at variables speeds and distances from the source and will deposit on the sea floor. Over time, this deposition will cause a complete coverage (blanketing) of the seafloor and most of the associated fauna.

So far, this blanketing effect has only been qualitatively investigated in small disturbance experiments on the basis of image analyses of the sea floor, without quantitative data on the relation of microtopography of the manganese nodules with the associated hydrodynamics environment. The aim of this contract is therefore to gain more precise knowledge using in-situ samples. Four scenarios were investigated which lead to blanketing effects.

A. A scenario right behind the collector with a concentration ~10 g/L, at an average shear rate of 1 s^{-1}
B. A scenario right after a reinjection with a concentration ~10 g/L, at a shear rate of 0.1 s^{-1}.
C. A scenario in the middle of the plume with a concentration ~1 g/L, at a shear rate of 0.1 s^{-1}
D. A scenario of remaining background plume, when most of the aggregation had taken place with a concentration ~30 mg/L, at a shear rate of 0.1 s^{-1}.

Approach and boundary conditions

The results should describe the characteristics of a plume at three different locations around a mining vehicle and at the reinjection point at midwater depth. Concentrations are given in g dry weight per liter.

Shear rates (G s^{-1}) were corresponding to free stream velocities of

A: 0.1G ≈ 3.5-4 cm/s (average flow velocity at the mining site; $u_* \approx 0.2$ cm/s);
B: 1 G ≈ 15 cm/s (flow velocity of an eddy passing through the mining site; $u_* \approx 0.9$ cm/s)

Experiments were carried out at salinities of 35 and ambient temperatures of 2-6 ° C.

2. Methods

Aim of this study is to simulate a dispersal of sediment plumes of three different particle concentrations (0.03, 1, 10 g/L dry weight) into the benthic boundary layer at the NORI site. For the process of aggregation

and to produce enough material for flume experiments with manganese nodules we use a water column simulator (Sanford, 1997). For experiments on blanketing and erosion under different flow conditions a seawater flume is used (Garcia & Thomsen, 2008). Experiments were run in triplicates.

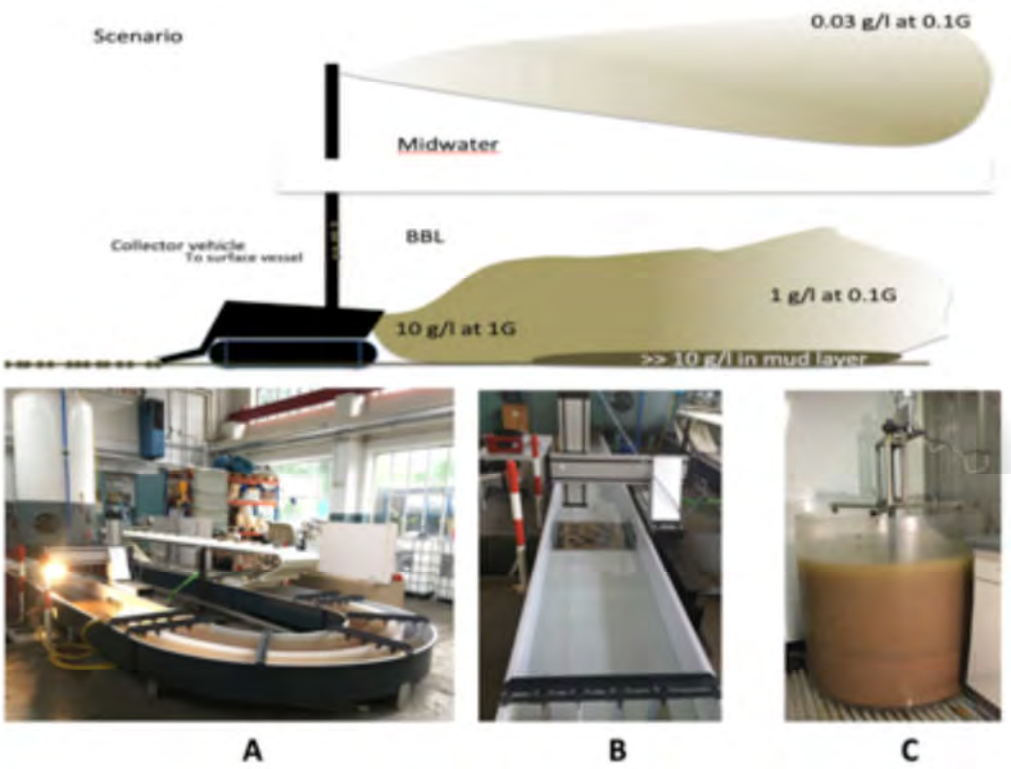

Fig.1. A,B: Seawater flume (16 m) with 0.25 m^2 test section; C: Water column simulator (1000 l)

Arrival of samples

MUC samples without nodules were sent from BlueField and arrived April 15. 310 kg of boxcorer samples from AllSeas arrived on Wednesday, May 6 together with 110 kg of manganese nodules. Samples were stored in a cool room at ≈ 3°C. Experiments and analyses started, after the temperature of the sediments had reached those of the cool room. The project report was due 3 months after arrival of sediments and nodules.

Selection of samples

Polymetallic nodules from the CCFZ NORI site were used to represent a typical exploration site of ≈ 16 kg wet weight. Type 1 nodules representing 90 % of samples taken from the NORI – D site were used. These Type – 1 nodules are unimodal and tightly dispersed around a mean of 2 – 3 cm. A figure with the typical size distribution of Type 1 nodules from a "2019 resource update" was provided by Anthony O´Sullivan on June 9. From the nodules provided by AllSeas on May 6, a total of 286 nodules (≈ 90 % of all fully intact nodules in the 110 kg sample) were selected carefully to generate a similar size distribution and placed in a 0.12 m^2 box prepared with original sediments (Fig.4). Each nodule was placed into the sediment with the correct side up (hydrogenic nodule growth side) and embedded down to the mark showing the sediment water interface. The sample, hereafter called "Type1 nodules" were then transferred into the test-section of the flume (Fig.5).

The following sediments were then separated for analyses: BC-094 and BC-110 which represent Type 1 nodule sediments and BC-124 representing Type 3 nodules. Only triplicate sediment samples from the top layer (0 - 15 cm) were analyzed. Those characterize sediments removed during mining operation. For the experiments we needed tens of kg of (near) surface sediments from stations with type 1 nodules. 0- 5 cm sediments from other stations were available but not at that amount.

2.1. Analysis of plume behavior

Particle sizes analysis

A modified combined approach using a LISST-100X (Laser In-Situ Scattering and Transmissometry. Sequoia Scientific) coupled with an industrial camera (DFK 23UX174, The Imaging Source) mounted with a telecentric lens (TEC-M55MPW, Computar) (Fig.1) was used to determine the sediment particle sizes (Mikkelsen *et al.*, 2005; P.S. Hill *et al.*, 2013). When combined with a particle camera, this set up allowed to detect a broad range of particle sizes ranging from 2.5 microns up to couples of millimeters (Gillard et al., 2019).

Step 1: Particle size and composition

Sediments from the 3 different NORI sites were disaggregated and analyzed for the particle size distribution. Particle size analyses were performed according to Gillard et al., 2019. As results of the particle size distribution showed normal abyssal plain sediments of the CCZ without larger biogenic compounds (Gillard et al., 2019), no further microscopic analyses were carried out.

Step 2: Particle size behind the collector

Sediments from representative NORI box corers BC-094, BC-110 (Type 1 nodules) and BC-124 (type 3 nodules) were disaggregated using a strong centrifugal pump (3000 RPM) to simulate the transport through the collector under high shear.

Aggregation processes

Introduction to aggregation. Collision between suspended particles depends on the size/settling velocity distribution of the particles and on the movement of the water. In the water column, turbulence and differences between the settling velocities of particles are the dominant control on aggregation rates, which consist of three main processes. Firstly, particles must be brought into close proximity, a process named `encounter. Secondly, these particles must be brought into direct contact by the flow fields around them, a process called `contact. Finally, the particles must `stick together. The encounter rate is a function of particle size, settling velocity and turbulence, whereas contact and stickiness are efficiencies related to relative particle size and physicochemical properties of particles, respectively (Thomsen & McCave, 2000). Aggregation and disaggregation process of particulate matter occur continuously in the ocean.

Step 3: Aggregation

Aggregation due to turbulent shear

The water column simulator consists of an inner paddles slowly rotating in a cylinder (110 cm diameter), based on the design of Sanford (1997) at a temperature of 2.0 °C. Shear rates of 0.1 and 1 G (s^{-1}) typically found in the BBL at the CCFZ under normal condition (0.1 G) and during the transition of an eddy (1G) or

behind a mining vehicle were simulated. A turbidity sensor (Aqualogger 310TY, Aquatec) able to reach maximum concentrations of 40 g/L (d.w.) was calibrated using the BC sediments provided by DG and used for particle concentration. A total of 200 to 2500 particles were analyzed semi-automatically for each experimental setup on aggregation and particle size distribution, using the program Image-J (https://imagej.nih.gov).

Fig. 2. Experimental setup in cool-room and water column simulator with developing mud layer

Step 4: Settling velocities

The aggregate size vs. settling velocity relationship is determined using a temperature-controlled settling column developed by Gillard et al., 2019. The column is designed to be operational under constant temperature (cooling system) and able to be mounted and on the LISST-100X for fine particle settling speed determination. The particles are 360° up-illuminated and settling rates vs. particle sizes are determined with a high-resolution camera. The post processing method is applied using the software ImageJ (https://imagej.nih.gov) which allows to investigate the settling speed and trajectory dynamics (Fig. 3B) of hundreds of aggregates at microscale definition. Settling velocities were analyzed under increasing plume concentrations to estimate the importance of hindered settling with the subsequent generation of a fluid mud which would generate a gravity current under slope angles of > 1 °.

Data processing for evolution of D50 aggregate size over time.

All analyses were carried on using MATLAB 2019b.

The grid of the X axis (time) was made in 1 min step intervals (240 in total).

1D cubic spline interpolation was used to fit the dataset, using not-a-knot end conditions. The interpolated value at a query point is based on a cubic interpolation of the values at neighboring grid points in each respective dimension.

A **B**

Fig.3. Settling column (A), and particle camera (B) in the coolroom

Step 5: Blanketing effect generated by a settling sediment plume

The thickness of a blanketing layer was investigated using the large seawater flume (Fig.1C).

Fig.4. Test section, with 286 Type 1 nodules from the NORI exploration site (≈ 16 kg ww)

The blanketing layer thickness and 3D structures formed under 5 different scenarios are analyzed:

1. under 10 g/L plume concentrations at 1G in the water column (near field)

2. under 1 g/L plume concentration at 0.1 G in the water column (near field)
3. under ≈ 0.03 g/L plume concentration in a 50 m water column (far field) or re-injection point
4. under 0.01 g/L plume concentration in a 50 m water column (far field)
5. under 0.01 g/L plume concentration in a 25 m water column (far field)

After blanketing experiments a 3D scanner provided analyses on the thickness and structure of the settled plume on the manganese nodules. Samples from the mud layer were collected are stored in a cool room and could be send to Deep Green on demand for further analyses of the new sediment properties.

D. Topography and flow field measurements

The measurements of topography and flow field were made using an ADV Vectrino profiler (Nortek, R. G. A. Craig et al., 2011) mounted on a 3D arm (Isel) for precise location of each measuring points (Fig. 5). Measurements were carried on the Typ1 nodule sample and after the blanketing experiment to allow a quantitative analysis of the sediment thickness as well as the flow field variation once the plume had settled.

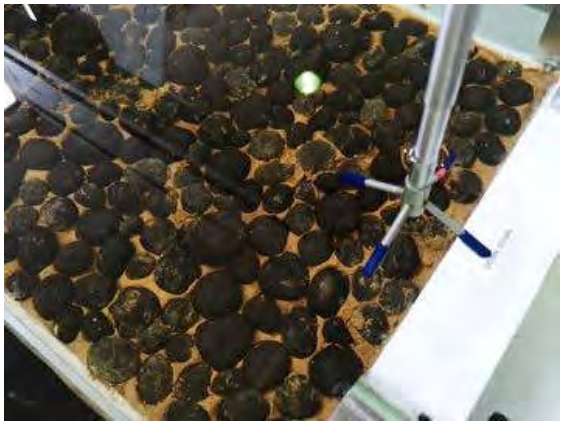

Fig. 5. Nortek Vectrino ADV profiler view into the test section of the flume

The micro-topography was mapped with the bottom detection capability of the instrument (10 Hz) and the Vectrino plus software (Nortek). MATLAB 2019b was used to compile the data and producing a first 3D mesh grid. This 3D mesh was further imported in MeshLab (www.meshlab.net, P. Cignoni *et al.*, 2008) for post-processing and texture layering. Overall, the measuring mesh grid was created from approximately 200,500 data points (6 hours per profile). The comparison between the original and blanketed sample was obtained using a 3D point cloud processing software CloudCompare (www.danielgm.net/cc).

Flow field measurements (200 Hz) were directly triggered by the Isel arm once it reached its measuring position. A grid resolution set to 6 mm in the XY direction and 7 mm in the Z direction was chosen for the ADV (signal to noise ratio) and overall profiling time (3 hours per layer profiled). In total, 5 layers above the nodule field were analysed. Overall, the 3D flow field mesh grid was created from approximately 13,500 measuring points. All datasets were transferred to Paraview software (www.paraview.org, A. James *et al*, 2005) which allow the visualization of combined topography and flow field measurements.

Step 6 Resuspension behavior of the blanketing layer under different flow conditions

The critical erosion velocity of plume sediments blanketing a nodule layer were analyzed. For that the plume

layer remained on the nodules under typical low flow velocities of 0.1 G (3.5 cm/s) for 4 hours and checked after 24 hours. Then the flow velocity was subsequently increased to 1 G flow (15 cm/s, passing eddy) to determine bedload transport and suspended-load transport. Photos and videos will be provided and analyzed. The approach is similar to the method published by Thomsen and Gust (2000).

Explanation-videos, photographs, processed data for the figures and tables will be transferred as supplementary materials onto a server provided by DG and available for download by September 15.

2. Results

A. Size distribution of disaggregated deep-sea sediments

The sediments samples (0-15 cm mixtures of the box cores BC-094, BC-110 and BC-124) were used for the experiments since they were available in larger amounts compared to MC samples provided by BlueField. The particle size distribution indicates that median particle size (d_{50}) was 12 µm, with the 25 % percentile at 3-4 µm, and 75 % percentile located at 26-29 µm and presented in the Fig. 6. Please note that these results do not necessarily resemble surface sediments, since they are a mix of the top 15 cm from these sites. Median particle size in these top 15 cm of sediments was lower than those from other sites at the BGR CCFZ (D_{50}> 20 µm, published) but similar to other parts of the BGR and Belgian sectors (D_{50} of around 8-25 μm).
Dry solid density of the sediments is expected to be ≈ 2400 kg/m^3 and a d_{50} of only 12 µm, with a bulk wet density of the upper 10 cm of sediments of ≈ 1230 kg/m^3.

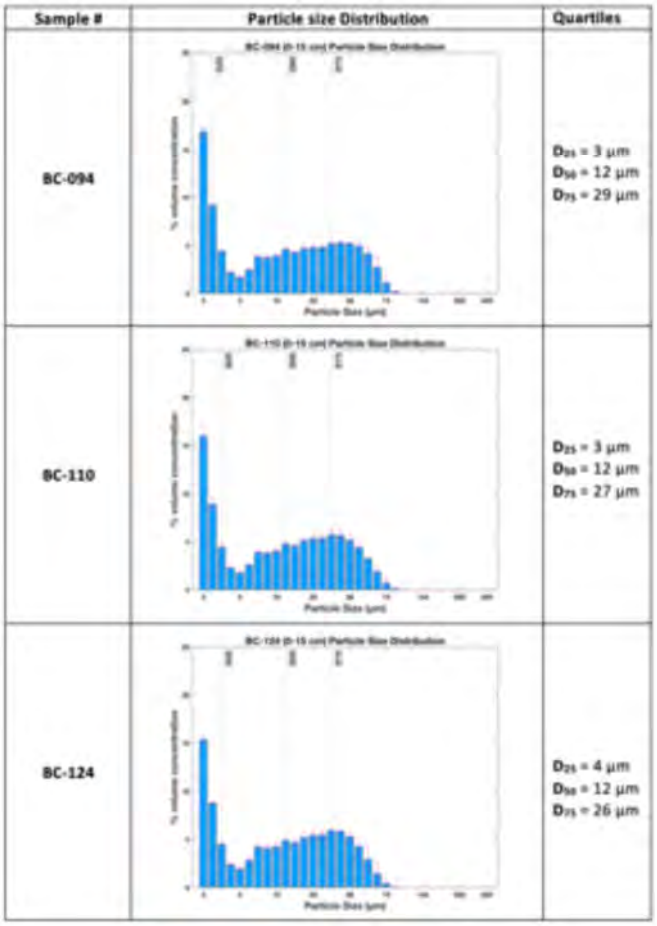

Fig. 6. Particle size distribution of NORI sediments used in this study.

B. Aggregation of 1 g/L sediment plume at a shear rate of 0.1 G (0.1 s^{-1}, ≈ 4cm/s flow velocity)

The Fig. 7 presents the conditions during the first 4 hours within a concentrated plume in a 1 m water column under shear rates of 0.1 s^{-1}. Three main flocculation phases could be identified (Gillard et al., in prep): the core aggregation, the export, the late aggregation.

The core aggregation phase 1 starts immediately after the plume is released. Within 30 min large aggregates are formed (confirming the result from Gillard et al., 2019). During that time, the size distribution of primary particles of d_{50} of 12 µm (Fig.6) rapidly shifts towards large aggregates with d_{50} of 680 µm (Fig. 7 I, blue line, d_{75} of > 1000 µm, pink area). This phase of constantly growing aggregates appears during the first 30 min (Fig. 7 I) and would continue during a permanent release of a plume, while simultaneously these particles are settling (exported) towards the seafloor. During this time, an export of ≈ 50 % of the initial plume concentration) down to ≈ 450 mg/L can be seen (Fig. 7 III, IV). Note that figures 7 III, A-F show the vertical particle concentration profiles within the 1 m water column, while Fig. 7 IV shows the change of particle concentration at 50 cm water depth (mid height of the water column simulator).

Phase 2, the export phase is characterized by decreasing aggregate sizes (Fig.7 I) and occurs between 30 and 120 min, as showed in fig. 7 I. During that phase, when particle numbers (indicated by particle concentrations) needed for aggregation rapidly decrease as a result of the fallout of large aggregates, the d_{50} of newly formed aggregates decrease from 680 µm to 280 µm while almost 90 % of the plume has settled to the bottom of the water column simulator after 60 minutes. This outcome shows that aggregates created at one concentration will change their size with a decrease in concentration even when the mixing conditions remain constant. The duration of the export phase (120 min in this case) which already starts immediately after plume release via aggregation and subsequent fallout is dependent on the water column height. A constant release of additional plume water would extend this core phase, however after a stop of such a release the export phase would occur in a similar time frame. In the case of this experiment after 120 min the overall plume concentration dropped to 72 mg/L.

The late aggregation phase spreads from 120 min onward. During that time the plume export slows down as the remaining particle concentrations in the water column have drastically decreased. At the end of the experiment (4 hours), the particle concentrations in the plume had been reduced from 1000 mg/L at the release to ≈ 50 mg/L. Even after 24 hours, the analysis of the remaining suspended particles indicates the presence of aggregates > 200 µm (Fig 7 II) and the d50 is expected to increase again as a result of additional aggregation (see. Gillard et al., 2019 for details under low plume concentrations of < 200 mg/L). Those aggregates have been created over a long period under the remaining low plume particle concentrations. They have scavenged more of the fine fraction < 200 µm (Fig.7 II, at 1440 min, indicated by blue color) and can be exported over larger distances under the low turbulence of 0.1 G.

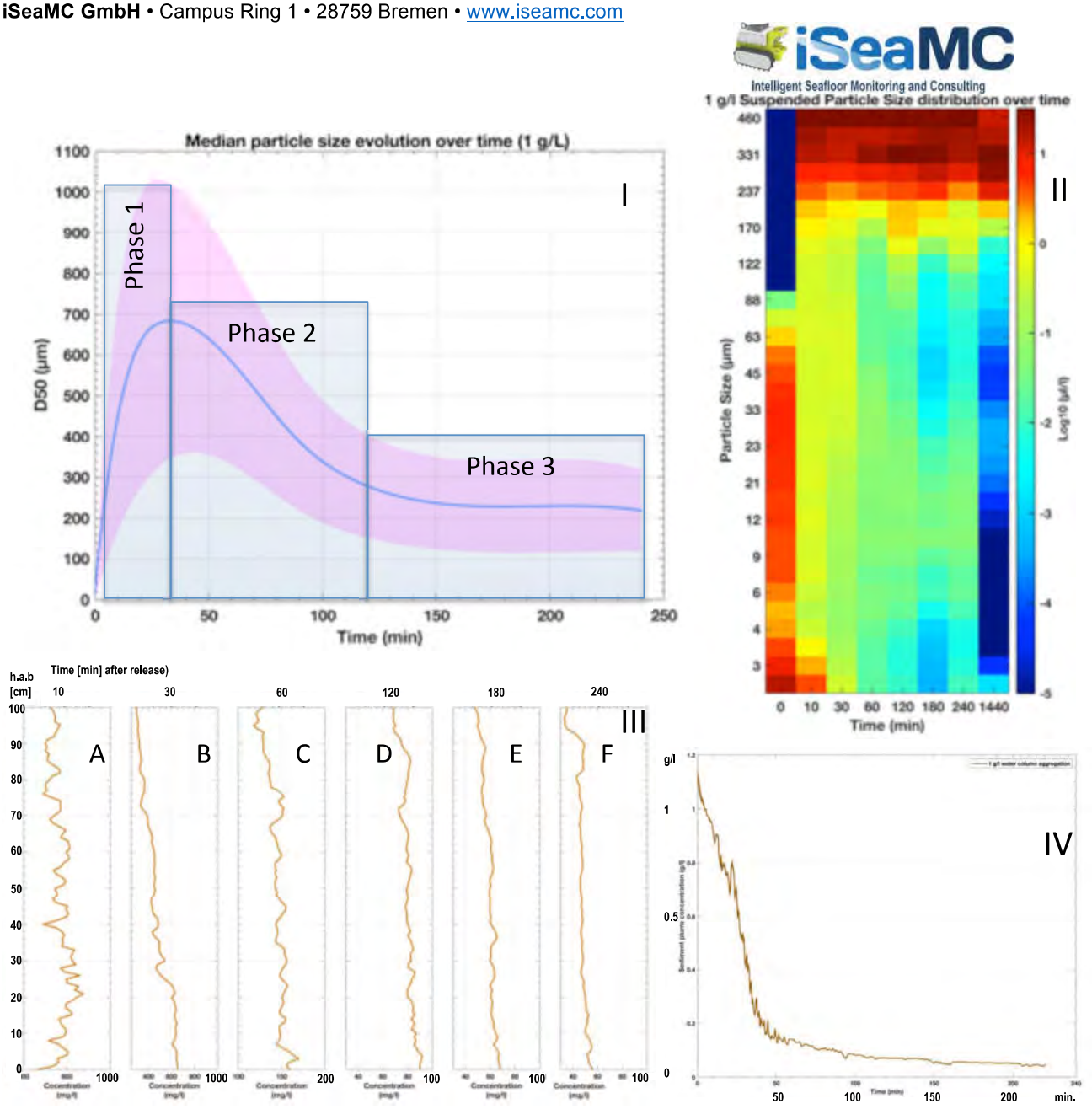

Fig. 7. Sediment plume aggregation dynamics at 0.1 G under 1g/L in the water column simulator.
I: d_{50} (blue line) ±STD (pink area) from particle camera data, analyzed with Matlab; II: determined by the LISST laser sizer at mid-height; III, IV: determined with Aqualogger turbidity meter (vertical profile run, run with Aqualogger at mid height)

C. Aggregation of 10 g/L sediment plume at a shear rate of 1 G (1 s^{-1}, ≈ 15 cm/s flow velocity)

The Fig. 8 presents the conditions during the first 4 hours within a concentrated plume of 10 g/L in a 1 m water column under shear rates of 1 s^{-1}. Under these 10x higher plume concentrations and higher turbulence, within 30 min after release the core aggregation phase results in large aggregates with d_{50} of 1900 µm (Fig. 8 I, blue line, d_{75} of > 2700 µm, pink area), while simultaneously these particles are rapidly settling (exported) towards the seafloor. Already after 30 minutes a mud layer of a few centimeter height with particle concentration ≤ 20 g/L begins to form (Fig 8 III). Within the main export phase (30 – 120 min after release) of decreasing aggregate sizes (Fig.8 IB) the d_{50} of newly formed aggregates decrease from 1900

µm to 300 µm while an almost 20 cm thick mud layer of unconsolidated particles of < 35 g/L has been formed (Fig. 18 III)

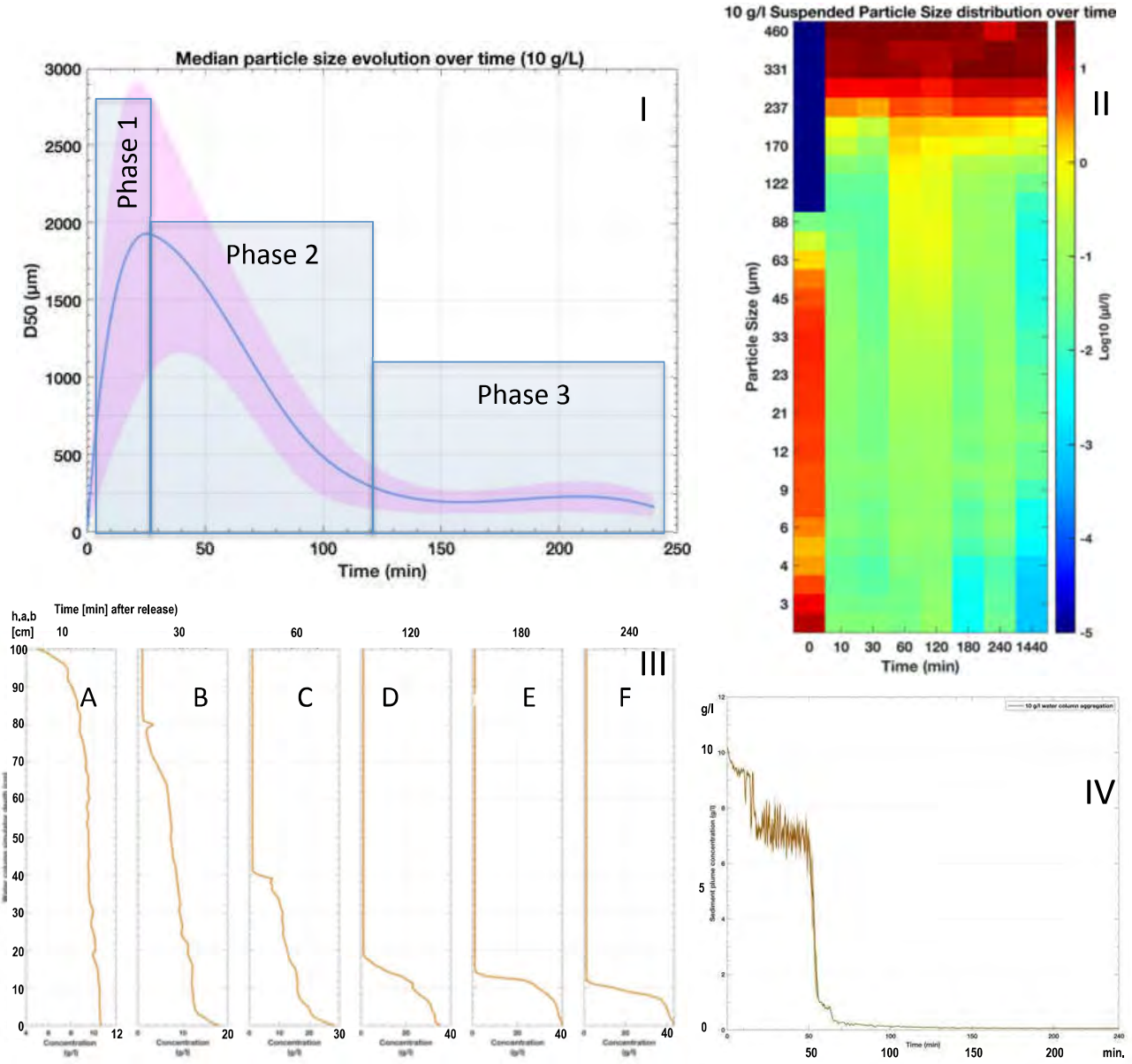

Fig. 8. Sediment plume aggregation dynamics at 1 G under 10g/L in the water column simulator.
I: d_{50} (blue line) ±STD (pink area) from particle camera data, analyzed with Matlab; II: determined by the LISST laser sizer at mid-height; III, IV: determined with Aqualogger turbidity meter (vertical profile run, run with Aqualogger at mid height)

The duration of the full export which already starts immediately after plume release via aggregation and subsequent fallout is dependent on the water column height. After 60 min, the overall plume concentration above the mud layer dropped below 10 % of the initial concentration of 10 g/L and is then expected to follow the process described for plume concentrations of 1 g/L but under higher turbulence. In fact, after additional 60 minutes the particle concentrations had dropped by another 90 %, following the behavior of the plume deposition of under 1 g/L. 240 min after the release of the plume a 10 cm thick and compacted mud layer with particle concentrations of 35 – 40 g/L (Fig. 8 III) has formed. Aggregates remaining in the water column resemble those detected under conditions of 1 g/L release in terms of particle size and volume

(Fig.7 II , 8 II, Log10 [µl/l]). Throughout the concentration drop under the two different initial plume concentrations, there is little difference between the aggregate sizes at a particular concentration, e.g., 100 mg/L. Since the main export phase ends already after 60 min when ≥ 90 % of the particles have settled at 10 g/L we used the 1 g/L at 0.1 G for interpretation of the 10 g/L scenario at 0.1 G. We then started additional experiments on hindered settling.

D. Settling velocities of individual plume aggregates in the settling column [w_s]

Curve fitted settling velocity (after Gillard et al., 2019)

Statistical analysis

The particle size and settling velocity datasets were first cleaned of extreme outliers (i.e. values higher / lower than 1.5 interquartile ranges above / below the 0.75 / 0.25 quartiles, respectively) and grouped by sediment concentration and by shear rate. Since particle sizes differed among the different groups, the measured velocities were normalized to the median particle size.

Modeling of settling velocities

A non-linear (logistic-sigmoidal) curve was fitted to model settling velocity against particle size for each concentration-shear rate combination, and 95 % confidence and prediction intervals were calculated based on each model. The curves followed:

$$y = \frac{a_1}{1+e^{\frac{a_2-x}{a_3}}}$$

where a_1 was the upper asymptotic limit of the curve, a_2 was the inflection point of the curve and a_3 a scaling factor for the size axis.

Modeled settling velocities for aggregates produced under 1 (A) and 10 (B) g/L

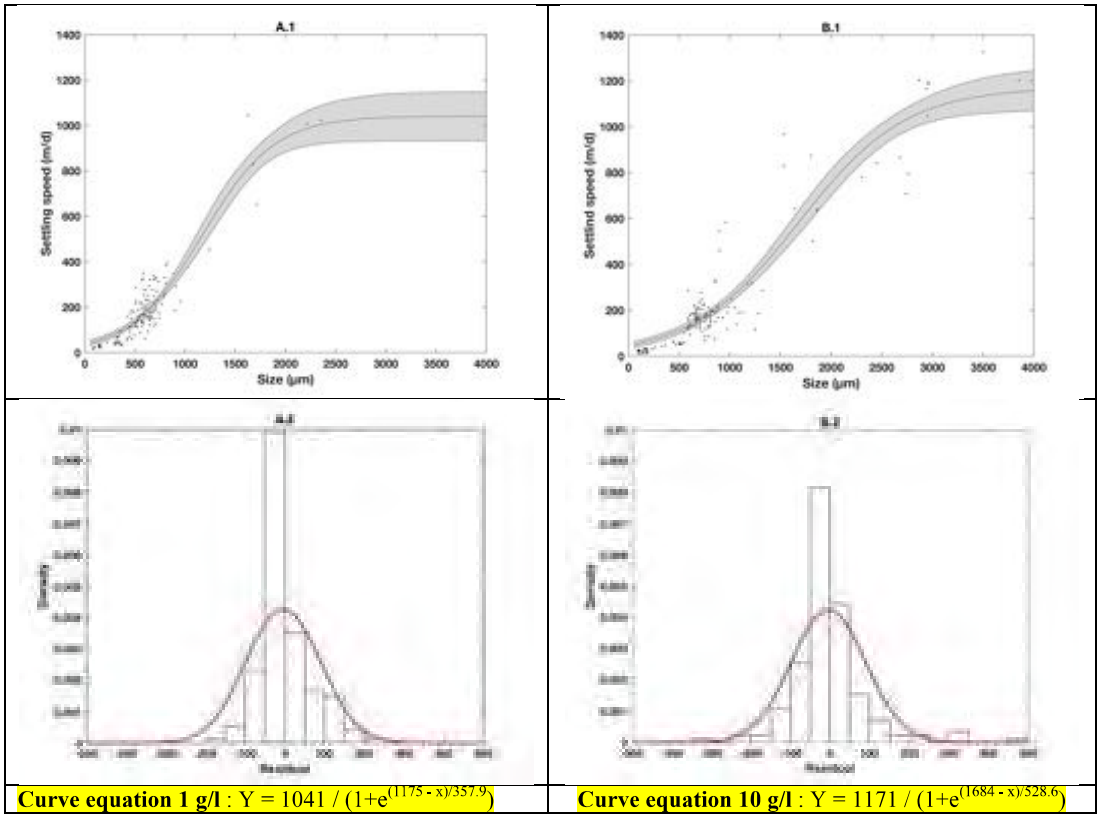

Fig. 9. Fitted model equation of settling velocities from deep sea sediment plume aggregates. Combined raw data and predicted model curve with corresponding 95 % confidence interval of aggregates produce under sediment plumes of (**A.1**) 1 g l^{-1} under 0.1 G; (**B.1**) 10 g l^{-1} under 1 G. Bottom line model residual histogram with plotted normal curve distribution.

Modeled settling velocities for aggregates produced under 1 g/L at 0.1 G (A) and 10 g/L at 1 G (B) with regression line

The two-regression lines presented in the figure below are equivalent to the regression line proposed for Deep-Green draft report figure 9. Figure A.1 correspond to 1 g/l experiment and B.1 to 10 g/l experiment.

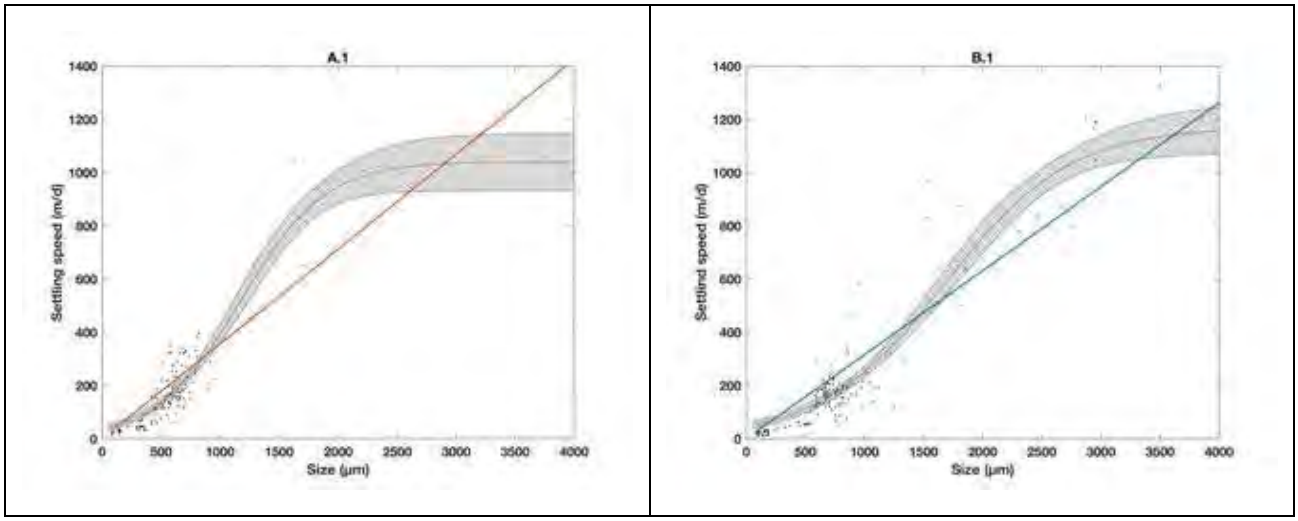

Fig. 10. Comparison with data from draft report (07.09.2020), where a linear relationship between size and settling velocity was calculated.

Comparison of settling velocity with Gillard *et al.* 2019

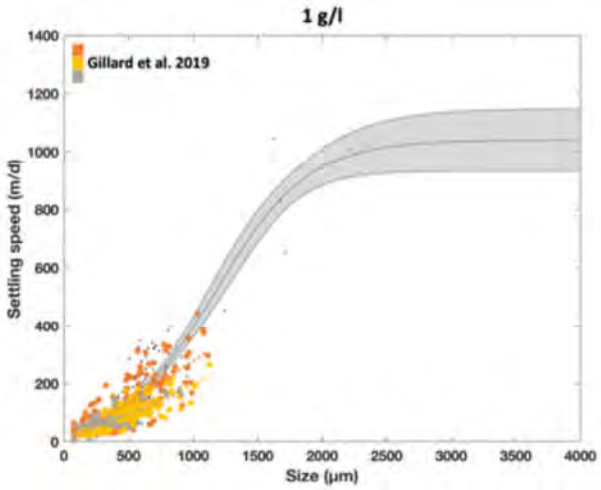

Fig. 11. Comparison with Gillard et al. 2019 data from BGR. Orange: 105 mg/L

Based on the observation that the d_{50} of BGR sediment was bigger than Deep green sediment, for equal shear rate and aggregate size, more particles will be incorporated into aggregates at the NORI site. This will result in denser particles of higher settling velocities.

Calculated specific settling velocities, typically expected at a midwater injection point with elevated turbulence

W_s at 1 g/L

The calculated settling velocities of aggregates at different times of the experiments (phases 1 – 3, see Fig. 7) varied for the d_{50} size between 67 and 209 m/d (Fig. 9). As expected, Ws increased during the first 30 minutes when aggregate size increased during the "core aggregation" phase. Between 60 and 120 min after release of the plume, when > 90 % of the flocs had already settled through the 1 m thick water column, both aggregate size and corresponding settling velocities decreased accordingly. However, after 24 hours size median floc size and settling velocity had increased again. This is the result of an ongoing aggregation process in phase 3 (late aggregation), when large aggregates are still in suspension and scavenge the still existing fine fraction in the water column.

It is worth pointing out that the aggregates formed during the "core aggregation phase" (phase I in fig. 7, 8) during the first 30 minutes might not follow the trend in size/settling velocity relationship between 30 to 240 minutes. Smaller aggregates are characterized by lower settling velocities and follow the lower end of the curved d/ws relationship shown in figure 10. This behavior was also visible in other studies (see Fig. 4 of Gillard et al., 2019). Thus there is obviously a difference in the d/ws relationship during the initial aggregation process (phase I) when compared to the export phase (phase II), when aggregates had reached a maximum size under the given conditions of turbulence and particle concentration and settle out.

Settling also occurs already during phase I but the process of larger aggregate formation obviously results in comparably lower settling velocities. This is possibly the result of compaction and subsequent increase in excess density of the aggregates during an increasing encounter rate; but more likely the increasing scavenging rate of the porous aggregates. Larger particles can be much more important in scavenging smaller ones if they are porous (Stolzenbach, 1993) and if they entrain small particles into their wakes as they settle (Hill and Nowell, 1990), as these mechanisms increase the collision efficiency. Thus with each scavenging process of larger aggregates which settle faster or collide with the very fine original sediments (d_{50} of 12 µm at the NORI site), the excess density of the aggregates increases which results in elevated settling velocities. This however should be further investigated but should not concern DHI, since you are mainly interested in phase II and III (Fig. 7,8) to simulate an ongoing plume injection.

For modeling purposes DHI should focus the export phase only, when the newly formed aggregates do not grow in size any more but settle out while scavenging the remaining fine fraction of the initial fine fraction of d50 = 12 µm.

W_s at 10 g/L

At 10 g/l initial plume concentration the settling velocities of individual aggregates in the settling column at different times of the experiments (phases 1 – 3, see Fig. 8) varied for the d_{50} sizes between 62 and 705 m/d. The same trend in Ws during the first 30 minutes was detected when aggregate size increased during the "core aggregation" phase. Again, after 24 hours the median floc size and settling velocity increased again, when even more large aggregates were still in suspension and scavenged the still existing fine fraction in the water column (see also Fig 8, II).

These results must however be interpreted with caution, especially when intended to use for particle transport models under high plume concentrations !

Table 1A. Size distribution and corresponding calculated specific settling velocities of individual aggregates of decreasing plume concentrations from initially 1 g/L over time (T) in minutes. See numbers in brackets [1], [2] to compare similar sized aggregates

	1 g/L							
	Unit	**T=10**	**T=30**	**T=60**	**T=120**	**T=180**	**T=240**	**T= 24h**
	Particle Concentration [g/L]	**0.911**	**0.427**	**0.140**	**0.072**	**0.053**	**0.046**	**0.008**
d_{25}	**µm**	294	465[1]	279	199	161	154	282
d_{50}		448[1]	681	386	278	228	218	326
d_{75}		671[2]	933	506	370	313	289	375
Ws_{25}	**m/d**	81.8	125.9[1]	78.7	63.9	57.8	56.7	79.3
Ws_{50}		**120.7**[1]	**209.2**	**103.4**	**78.5**	**68.9**	**67.2**	**88.8**
Ws_{75}		204.6[2]	350.9	139.1	99.3	85.9	80.8	100.6

Table 1B. Size distribution and corresponding calculated specific settling velocities of individual aggregates at decreasing plume concentrations from initially 10 g/L over time (T) in minutes. Note that these results show the behavior of particles above a fluid mud layer.

	10 g/L							
	Unit	**T=10**	**T=30**	**T=60**	**T=120**	**T=180**	**T=240**	**T= 24h**
	Particle Concentration [g/L]	**9.368**	**6.559**	**0.767**	**0.079**	**0.058**	**0.052**	**0.007**
d_{25}	**µm**	863	1292	430[1]	213	157	122	318
d_{50}		1378	1902	641[2]	296	206	161	371
d_{75}		2085	2395	830	412	268	208	437[1]
Ws_{25}	**m/d**	204.5	377.8	99.9[1]	68.2	61.7	58.0	82.2
Ws_{50}		**420.6**	**704.6**	**142.9**[2]	**79.0**	**67.4**	**62.2**	**90.2**
Ws_{75}		797.5	929.0	194.2	96.8	75.2	67.6	101.1[1]

After ≈ 120 minutes, when most of the particle fallout had taken place under different initial particle concentrations, subsequent settling velocities of both particle groups were similar.

These settling velocities should be used for particles settling above the fluid mud layer or at a midwater injection point.

The particle concentrations of 0.007 and 0.008 g/L after 24 hours of aggregation and subsequent export are low. The increase of aggregate size between 3 and 24 hours after injection can however be considered as a relevant process during the settling of the remaining aggregates through a water column even at such low particle concentrations. The particle concentrations for the CCZ in the lowermost 10 m water column are in the order of < 100 µg/L (Gardner et al., 2018). For midwater conditions there are very few data available but own results from particle camera deployment show particle numbers around 100 - 300 particles /L, which can be a few hundred µm in size (Gillard, in prep). Aggregate studies at continental margins at 4000 m depth revealed particle concentrations in the BBL of ≈ 3 mg/L, with aggregates of d_{50} of 300 µm and N of 200 – 300/L. Under these particle concentrations scavenging of 10 µm particles is unlikely, especially when the larger particles are low in organic content. However, an incoming pulse of phytodetritus can clear out water layers of 7 – 8 mg/L (Thomsen & McCave, 2000; Hill and Nowell, 1990). Since the NORI site is located at the eastern part of the CCZ (vanReusel et al., 2016), pulses of organic rich phytodetritus can be expected and this would have an impact even on such comparably low particle concentrations of 7 - 8 mg/l, which are still 1-2 orders of magnitude higher than the background value for the Pacific. It is therefore recommended to estimate the newly formed background concentration of fine particles in suspension which will disperse in the Pacific Ocean after large scale midwater injection from mining operations has started. The background values will slowly increase over time (1 – 20 years of operations). However, if the modeling of DHI shows very low particle concentrations of ≈ 100 µg/L for the far field site around an injection point and this can be verified during onsite experiments, I would not expect a significant impact on the vertical migration behavior of zooplankton. One can however expect that research institutions, NGOs and the ISA will be very skeptical towards these modeling results, especially since recent discussions between ISA, potential contractors and the science community favor the reinjection of the return low behind the collector. This however could dilute the concentrated plume behind the collector. One contractor claims to invent an additional concentrator, which produces nodule sized sediment pellets. I have however not seen any evidence for that. It is also important to point out that even under a turbulence of 10 G, a plume of 0.5 g/L produces aggregates of at least 600 µm in size within the first 10-15 minutes (Gillard et al., 2019, Fig. 3).

E. Effective settling velocities [w_s] of populations of plume aggregates in the water column simulator: settling inside a developing fluid-mud layer, typically expected behind the collector

While the above mentioned results are normally used for numerical modeling of plume dispersal, we also applied another approach to better understand the behavior of concentrated plume injections ≥ 1g/L in the BBL near the seafloor for comparison. For that we used the data from the Aqualogger turbidity meter, which automatically adapts to increasing particle concentrations. The calculated settling velocities presented below describe the behavior of a floc population. Theory (after Dankers & Winterwerb, 2007): the single floc settling in still water (see table 1) has a specific settling velocity, which is a function of its shape, size, density and the viscosity of the fluid. When the concentration of particles increases, they start to interfere and hinder each other, thereby reducing their settling velocity (see also video). This is called hindered settling and the settling velocity is referred to as the effective settling velocity. When the concentration increases further, the particles tend to be in constant contact with each other, and a particle framework builds up. The change from a water supporting system to a sediment supporting system is called gelling when early consolidation starts.

W_s at 1 g/L

The effective settling velocities of the floc population was calculated via the particle concentrations from the vertical profiles in the water column simulator and from sing point measurements at 50 cm water depth. The initial settling velocities of the fast growing aggregates during the first 10 minutes after the plume was released was ≈ 0.1 cm/sec (86.4 m/day). Between 10 min and 30 min when hindered settling began, w_s was reduced to 0.03 cm/s (28.8 m/day). During the export phase 2 (see fig.7) w_s ranged between 0.01-0.02 cm/s (7.2 – 14.4 m/day). After 60 minutes > 90 % of the fallout has already occurred and all large aggregates had settled with w_s > 0.02 cm/s (> 14.4 m/day), Table 2A. Interestingly, the settling velocities determined via the water column simulator were significantly lower than those measured in the settling column. They represent the w_s of the floc population and not of individual aggregates, and the settling occurred under low turbulence of 0.1 G while the data on w_s in table 1 result from measurements in stagnant water of the settling column.

Table. 2A, 1g/L

Part.Conc [mg/L]	Minutes	w_s [cm/s]	w_s [m/h]	Settling velocity [m/day]
1165	0			
905	10	0.1	3.6	86.4
418	30	0.03	1.2	28.8
140	60	0.02	0.6	14.4
72	120	0.01	0.3	7.2
46	240	0.01	0.3	7.2

Ws at 10 g/L

The effective settling velocities of these flocs decreased from 0.1 cm/s during the first 30 minutes to 0.02 cm/s after 60 minutes when > 90 % of the fallout has occurred. These significantly lower settling velocities during the first 30 minutes are the result of hindered settling which definitely also occurred right above and within the thickening mud layer and resulted in a further reduction of the settling velocities of the incoming aggregates to 0.006 cm/s, Table 2B. The difference between Ws measured in the settling column and via water column simulator is even more pronounced at 10 g/L. Settling velocities per day are almost two orders of magnitude lower during the first 60 minutes. The data in table 2 represent the settling behavior of groups of flocs (floc population) and not individual ones (Table 1) and were determined under turbulent flow of 1 G (15 cm/s flow velocity). These results should give DG a first insight, how the plume is dispersed and settles under high concentrations in fluid mud and numerical modeling of sediment transport should take this into account. Videos are provided from these experiments for discussion with your modeler team.

Table 2B, 10 g/L

Part.Conc [mg/L]	Minutes	w_s [cm/s]	w_s [m/h]	Settling velocity [m/day]
10170	0			
7033	30	0.01	0.4	9.6
770	60	0.02	0.6	14.4
80	120	0.01	0.4	9.8
60	180	0.01	0.3	6.8
50	240	0.006	0.2	5.2

Comparing the size and settling velocities of aggregates under the two different initial plume concentrations

reveals that higher concentrations of 10 g/L result in larger floc size but these populations of larger flocs settle with lower settling velocities under conditions of hindered settling and turbulent flow. At 1 g/L plume concentration under normal deep sea flow conditions of 0.1 G (≈ 4 cm/s), the settling velocities determined in the water column simulator under low turbulence of 0.1 G during the initial phase of aggregation are at least more comparable to those from the stagnant settling tube for similar d_{50} values (see table 1, d_{50} after 10 and 180 minutes); however it strongly deviates from conditions of elevated plume concentrations (10 g/L) and elevated turbulence (1G). The lower settling velocities of larger flocs during the core phase of aggregation at 10 g/L is a combination of both, hindered settling and elevated turbulence. Hindered settling starts when large flocs at high concentrations hinder each other in settling (see 400 MB video of 10 g at T30, provided in September or on demand). In the video, large aggregates are visible which constantly form larger or smaller units after they get in contact with others and are clearly hindered in settling). This behavior is known from studies in sediment transport and stated to start at concentrations between 1 to 15 g/L. Increasing turbulence is also expected to keep the flocs in suspension for longer periods and decrease the averaged settling speed of a floc population, especially when compared to results from stagnant settling columns (Tran et al., 2018). We are offering support to your modelers and AllSeas for potential recommendations on how to handle the collector exhaust pipe in order to influence a forming mud layer.

Similar effective settling velocities of 0.01 – 0.02 cm/s for floc populations have also been experimentally determined by Dankers & Winterwerb (2007) for highly concentrated mud suspensions under hindered settling (called settling suspensions in hindered settling regimes). Table 3 summarizes the settling (fallout) times for floc populations using the results from the water column simulator. During the first 120 minutes (data from 30, 60, 120 minutes) of deposition averaged values of a ws of 0.02 cm/s for 1 g/L at 0.1 G and 0.013 cm/s for 10g/L at 1 G (both using data from table 2) **are used for the fluid mud layer which rapidly develops**. It is important to note that hindered settling under plume concentrations of both 1g/L and 10 g/L consequently results in extended travel times which carry the plume particles over larger distances away from the injection point. If we assume a plume injection of 1 g/L under low flow conditions of 0.1 G at a height of 10 m above the sea floor (Table 3, [1]) and an export phase with settling velocities of ≈ 0.02 cm/s for the floc population in the fluid mud it would take approximately 14 hours for a > 90% fallout through the full 10 m water column. These particles would travel over distances of 1.8 km. Extended distances of 7.5 km would occur under the flow velocities of 1 G (15 cm/s; deep sea eddy). Increasing concentrations in the mud-layer would also lead to gelling and subsequently lower settling velocities. It is important to note that dispersal via turbulence would increase the settling velocities again, when aggregates switch from hindered settling to individual settling; and the formation of a density currents **could drastically speed up the horizontal export velocity**. The fluid-mud would then be exported along a slope or through a gulley into a depression on the seafloor, possibly kilometers away. **If the area B on figure 21 (p.28) shows such an area of seafloor depression (valley, M.Clarke, pers.comm.), we would recommend to start modeling gravity plumes for a harvesting site north of that area for use as potential plume dump site.**

Table 3. Time for the fallout of 90 % of the plume particles under 0.1G and 1G conditions from different plume injection heights into a fluid mud layer assuming an average fallout velocity of A: 0.02 cm/s (1 g/L scenario) and B: 0.013 cm/s (10 g/L scenario) and that such fluid mud layers have a maximum height of 10 m.

A: Ws of 0.02 cm/s	Minutes to settle	Hours to settle	Days to settle	Travel distance (km) at 0.1 G	Travel distance (km) at 1 G
1 m	83	1.4	0.1	0.2	0.8
5 m	417	6.9	0.3	0.9	3.8
10 m [1]	833	13.9	0.6	1.8	7.5

B: Ws of 0.013 cm/s	Minutes to settle	Hours to settle	Days to settle	Travel distance (km) at 0.1 G	Travel distance (km) at 1 G
1 m	128	2.1	0.1	0.3	1.2
5 m	641	10.7	0.4	1.3	5.8
10 m [2]	1282	21.4	0.9	2.7	11.5

Under scenario B in table 3 (10 g/L, [2]) it would take 21.4 hours for a 90% fallout through the full 10 m water column. Under these flow conditions particles would travel over distance of 2.7 - 11.5 km.

Settling within the mud layer

Aggregates formed under elevated plume concentrations develop a different settling behavior and cannot be described via individual aggregates but rather as a floc population (see 2.2 Aggregation dynamics). The sedimentation under 10 g/L in a 1 m water column or 1 g/L in a 10 m water column cause the formation of a fluid mud layer with concentrations rapidly exceeding 30 g/L (Fig.8, III). The settling velocity of the floc population within the mud layer was strongly decreased and can be estimated by measurements of the compaction of this layer. Fig 12 shows the rapid sedimentation of aggregates under different particle concentrations during the flume experiments in a 16 cm high waterlayer above Type 1 nodules (Scenario 3-5). Within the first 5-10 minutes the sedimentation of the aggregating plume particles is characterized by rapid decrease in particle concentrations (see also Figures 7, 8 for 1 m) within the water layers above the Type 1 nodules in the seawater flume (Fig. 12). The much shorter clear-out time is the result of the lower water column (16 cm vs. 100 cm of the water column simulator). As shown in fig. 13 (scenario 3, 5 minutes after release), a mud layer is formed during these first minutes which can be characterized by an initial loose layer of incoming aggregates, which rapidly gets compacted by 75 % once the incoming aggregate flux diminishes (Fig 12, 13, scenario 3, after 10 min). After that, further compaction and consolidation of the newly formed mud layer is below 10 %. This change from a water supporting fluid mud system to a sediment supporting system is called gelling when early consolidation took place.

This mud layer would remain loose for hours or days at its top section and increasingly consolidated in the lower section until the incoming flux of aggregates has diminished. Figures 25 and 26 on page 26/27 show such a loose mud layer above the test section of the Type 1 nodules and in the water column simulator.

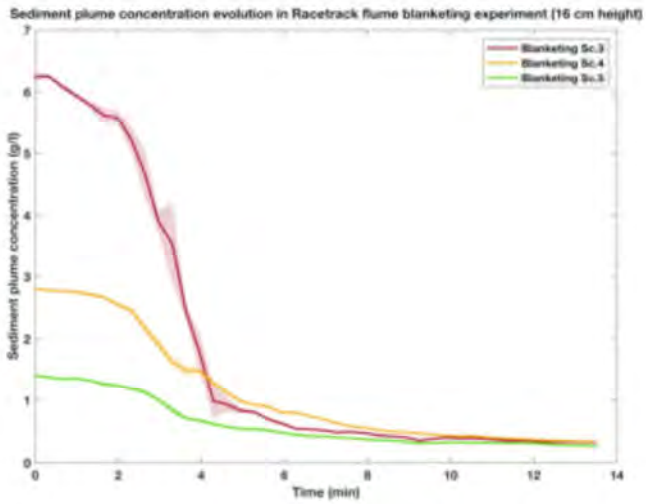

Fig. 12. Plume concentration (aggregation) during the first 15 minutes after release in three scenarios Sc.3: 1 g/L, Sc.4: 0.5 g/L, Sc.5: 0.25 g/L to simulate conditions in a 1 m water column.

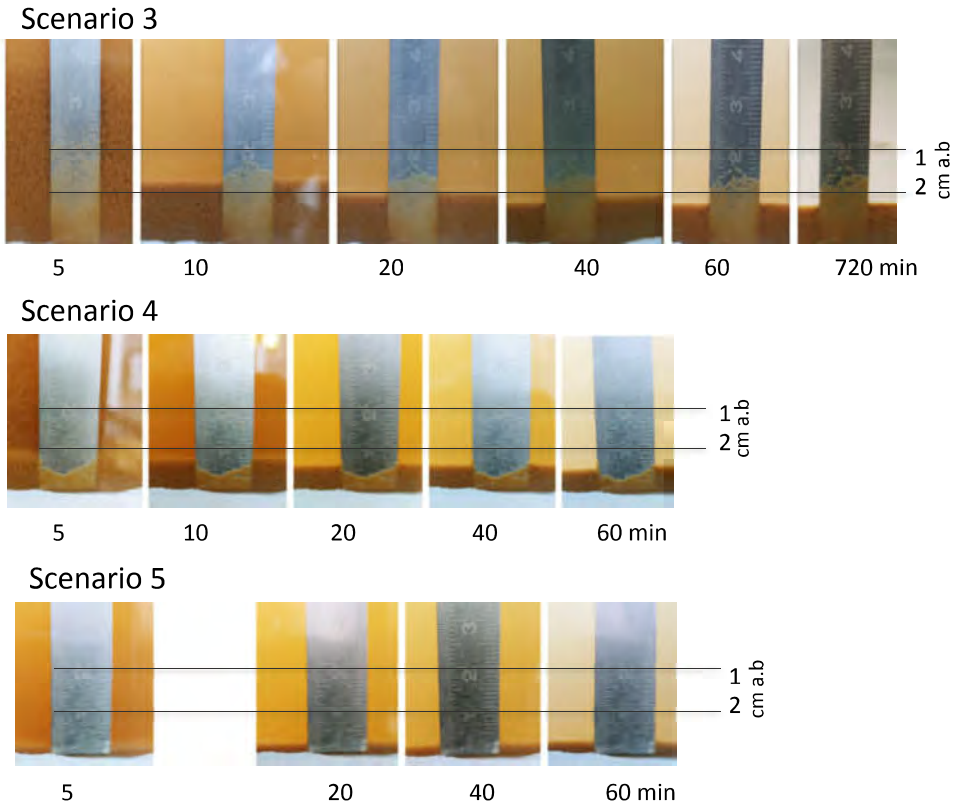

Fig. 13. Side view of test section of the flume showing the blanketing layer next to the window for better visualization. Note that a 3-4 mm have to be added to compensate for the silicone sealing next of the window. A-D is 5, 20, 60, 1440 minutes after release of the plume. For different concentrations of each scenario see Fig. 12.

E. Topographic analysis and quantification of the "Blanketing layer"

E.1 Original sample topographic analysis

The nodule field was scanned using an ADV Vectrino Profiler at (10Hz). Each scan took over 6 hours, and 200000 measuring points were collected. The final output results are presented in Fig. 14C. The use of an ADV over optical sensor such as a laser camera for 3D modeling of in-situ topography has revealed to be a powerful method and provides a new outlook for multi-usage of 3D sensors during mining activities.

The current resolution of the grid produced was X (0.47 mm), Y (1 mm), and Z (down to 10 µm). The output file (.ply) will be transferred to DG and can be easily opened with the open-source software MeshLab (www.meshlab.net; File --> Import Mesh). This will allow a 3D navigation inside the nodule field using the computer mouse.

Bottom elevation (Fig. 14B) determined by the 3D scan of the sediment surface revealed that the nodules created a microtopography which penetrated the bottom boundary layer [BBL] up to 16.8 mm with an average height of 8.6 ± 2.7 mm. Each nodule was placed into the sediment with the correct side up (hydrogenic nodule growth side) and embedded down to the mark showing the sediment water interface.

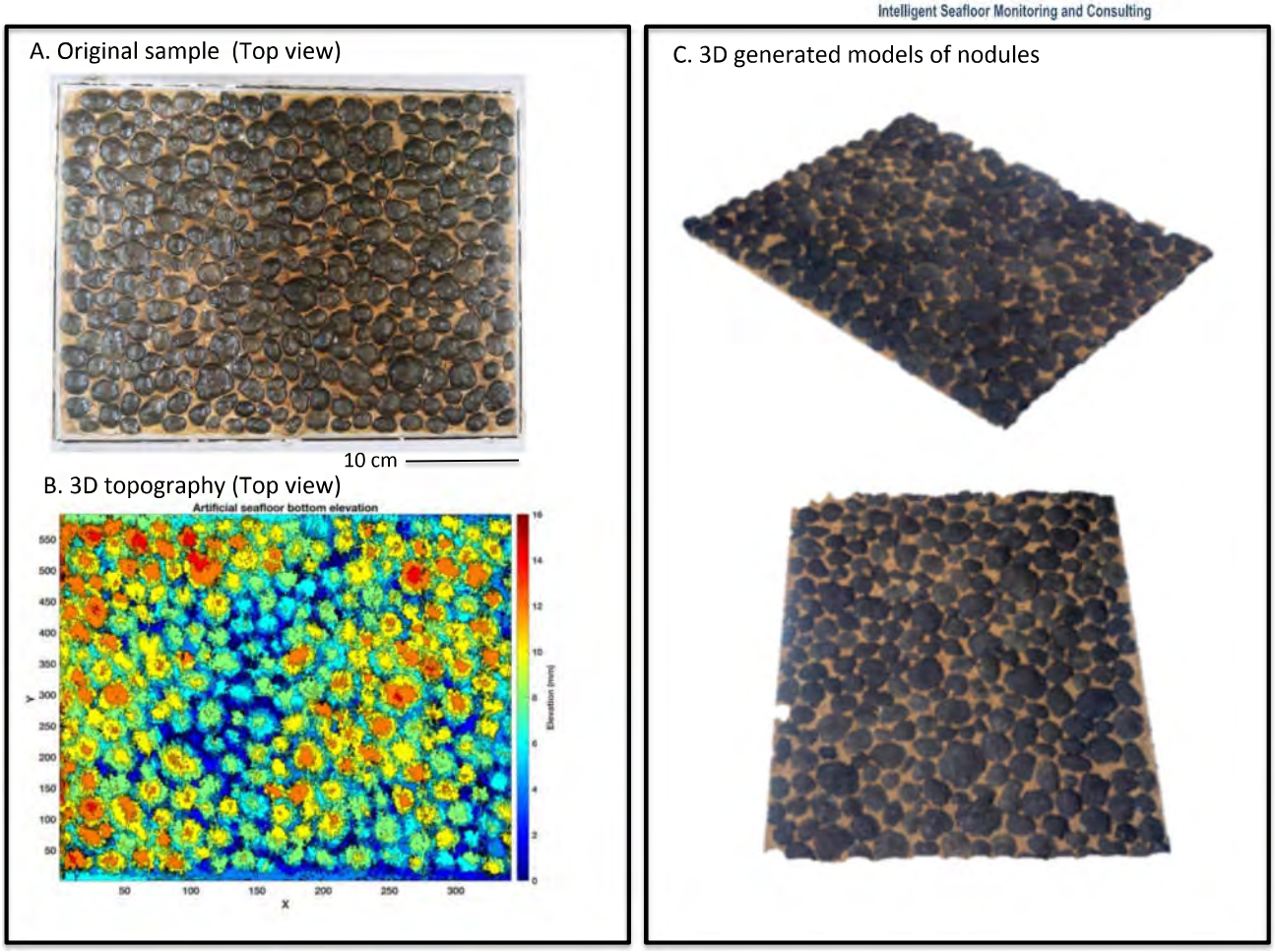

Fig. 14. 3D representation and microtopography of the Type 1 nodules.

E.2 Blanketing experiment

Fig. 15 shows the photograph and 3D map of the blanketing layer on the test section with Type 1 nodules after settling of a ≈ 1-meter height aggregated plume of 1 g/L (1000 g/m^3 see table 4, scenario 6). Bottom elevation (Fig.16 C) indicates that the topography of the nodule field has changed in comparison to the original sample (Fig.14 C). The Type 1 nodules were covered by a thin layer of plume particles and the microtopography surface became much smoother, as shown by both the pictures (Fig.15) and bottom elevation (Fig.16). All nodules were entirely covered by the deposited plume. Note that this occurs for any scenario with a blanketing layer of ≈ 11 mm (table 4, scenario 6). The shapes of the nodules are still visible under the newly formed sediment surface of the settled plume.

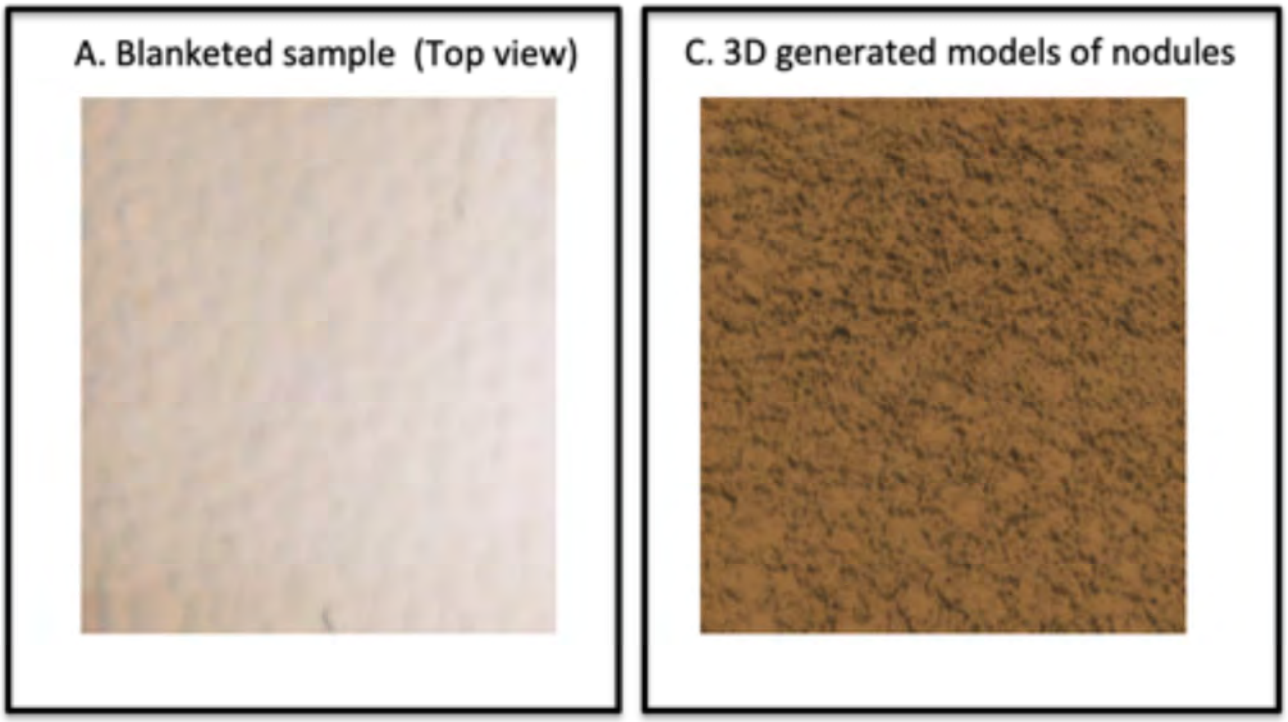

Fig. 15. Photography and 3D representation of the Type 1 nodule field.

A superposition between the original nodule's field and the newly formed blanketing layer is given in Fig. 17. Those results showed that the ADV sensor was able to precisely measure the newly form sediment bed and once more prove the efficiency of those instruments. The blanketing layer quantification was investigated based on a 3D cloud mesh comparison using the free software CloudCompare (See Method section). The blanketing thickness is shown as a color layer and plotted on the top of the original 3D grid of the Type 1 nodules for better visualization.

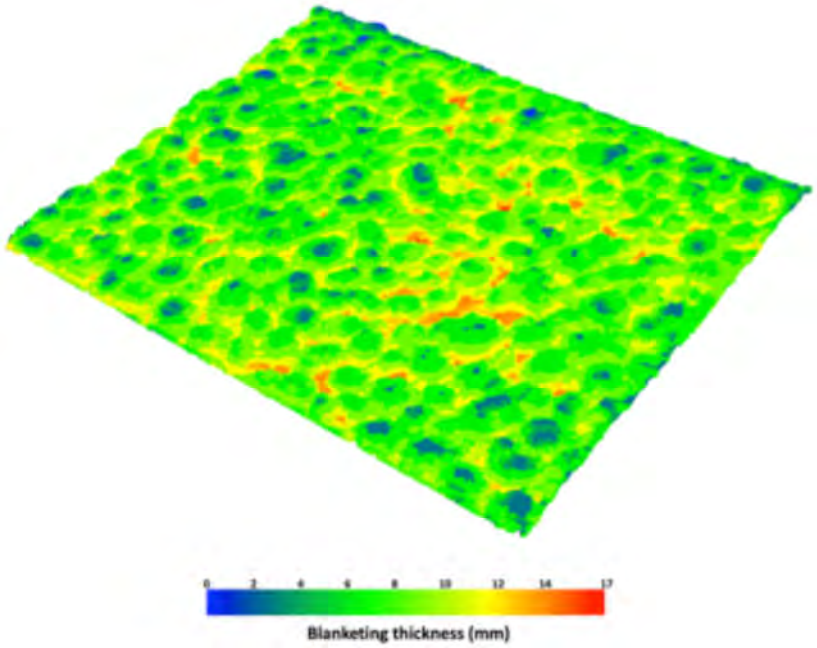

Fig. 16. Type 1 nodule blanketing thickness determined with the AV sensor. Average height of the Type 1 nodules into the benthic boundary layer was 8.6 ± 2.7 mm, with maximum height of 16 mm.

The average blanketing of the nodules ranged from 2 - 3.5 mm on top of nodules, which penetrated the BBL up to 16 mm to a blanketing layer of > 6 mm on top of smaller nodules. Decreasing nodule height (BBL penetration) resulted elevated blanketing. Increasing or decreasing the plume concentration will vary the blanketing layer accordingly.

E.3 Quantification of blanketing thickness

For the quantitative determination of the relationship between plume concentration at different heights above bottom [h.a.b] in g/m^3 dw (dry weight), the resulting sediment load on the seafloor (g/m^2) and the corresponding thickness of the blanketing layer (mm) three different approaches were used (Fig.17):
1. aggregated sediment plumes of known concentrations transferred by gravitation into test vials (series1, see fig. S3, p.27), 2. the isolated test section of the racetrack flume or 3. in water column simulator. The results are shown in Fig. 15 and table 4. The three different approaches resulted in very similar results. The blanketing layer thickness (mm) varied proportionally to the final accumulated sediment load (g/m^2) and allows to determine the blanketing effect of varying initial plume concentrations at different heights above the seafloor.

It is important to note that most data describe the blanketing up to a thickness of 16 mm, which would cover all Type 1 nodules at the NORI site. Higher blanketing loads are the result of high plume concentrations which would blanket and further compact. (see deviation from the linear regression lines presented in fig. 17 towards the green line which includes a 10 kg/m^3 blanketing effect).

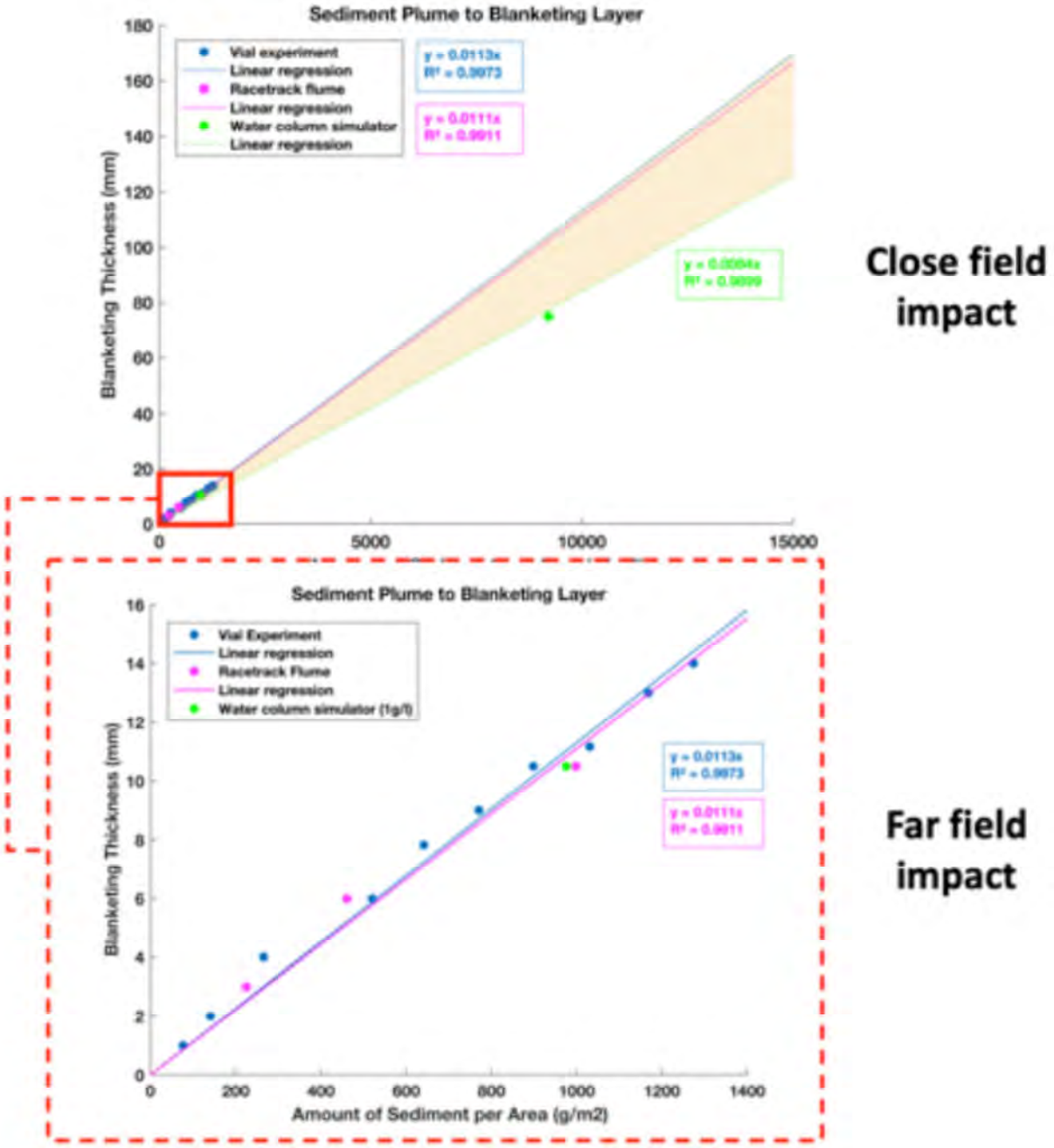

Fig. 17. Correlation between accumulated particle load on the seafloor and resulting thickness of the blanketing layer, as determined via three different experimental approaches.

Table 4. Thickness of the blanketing layer from different particle loads (g/m^2) on the seafloor using the correlation coefficients determined in Fig. 18 from the three different test scenarios.

[1]: 10 g/L plume concentrations at 1G in a 1 m water column (near field)
[2]: 0.03 g/L plume concentration in a 50 m water column (far field) or re-injection point
[3]: 0.01 g/L plume concentration in a 50 m water column (far field)
[4]: 0.01 g/L plume concentration in a 25 m water column (far field)
[5]: 1 g/L plume concentration in a 10 m water column (near field) or re-injection point
[6]: 1 g/L plume concentration in a 1 m water column (near field) or re-injection point

Blanketing [mm]	**g/m2 blanketing**	**g/m3 in water column**				
		1 m	**5m**	**10m**	**25m**	**50 m**
1	100	100	20	10	4	2
2	200	200	40	20	8	4
3	300	300	60	**30**	**12** [4]	6
5	400	400	80	40	16	8
6	500	500	100	50	20	**10** [3]
7	600	600	120	60	24	12
8	700	700	140	70	28	14
9	800	800	160	80	**32**	16
10	900	900	180	90	36	18
11	1000	**1000**[6]	200	**100**	40	20
12	1100	1100	220	110	44	22
14	1200	1200	240	120	48	24
15	1300	1300	260	130	52	26
16	1400	1400	280	140	56	28
17	1500	1500	300	150	60	**30** [2]
17	2000	2000	400	200	80	40
42	5000	5000	1000	500	200	**100**
84	10000	**10000** [1]	2000	**1000**[5]	400	200
420	50000	50000	10000	5000	2000	1000

F. Resuspension behavior under increasing flow conditions

Examples of the resuspension behavior of the blanketing layer after 12 or 48 hours of sedimentation on Type 1 nodules are presented in Fig. 18 under the three different scenarios (sc. 3,4,5; Fig. 12). Under flow conditions between 4 cm/s (0.1G, typical deep sea flow) and 15 cm/s (1G, simulation of a deep sea eddy) in sc.3, Fig 18, when the Type 1 nodules were completely covered by plume particles, no resuspension of the newly formed sediment surface took place. Only loose large aggregates which were not part on the original process of mud layer compaction were exported as bedload and suspended load. This would also be the case for an incoming flux or organic matter from the sea surface. The newly formed and almost flat sediment surface stayed intact.

Under sc.4 conditions of a thinner blanketing layer (Fig. 18) which still completely covered all Type 1 nodules (Fig. 18), erosion of the blanketing layer started at 9-10 cm/s at zones of enhanced turbulence either at the leading edgy of the nodule field and around only slightly covered nodules within the field. This erosion was further enhanced under flow velocities of 15 cm/s but did not result in large scale erosion of the blanketing layer during the following hours. Sc.4 represents a plume concentration of 500 g/m^3 in a 1 m water column or 10 g/m^3 in a 50 m water column (scenario [3] in table 4).

Under sc.5 conditions of an very thin blanketing layer (Fig. 18) which did not completely cover all Type 1 nodules (Fig. 18), erosion of the blanketing layer also started at 9-10 cm/s and was further enhanced under flow velocities of 15 cm/s, when an increasing number of larger Type 1 nodules were flushed and became visible again. Again, larger scale erosion of the blanketing layer did not occur during the following hours.
These results are different from type 2 and 3 nodules (as determined) for other projects, where large scale erosion around the nodules took place under these flow conditions of 15 cm/s.

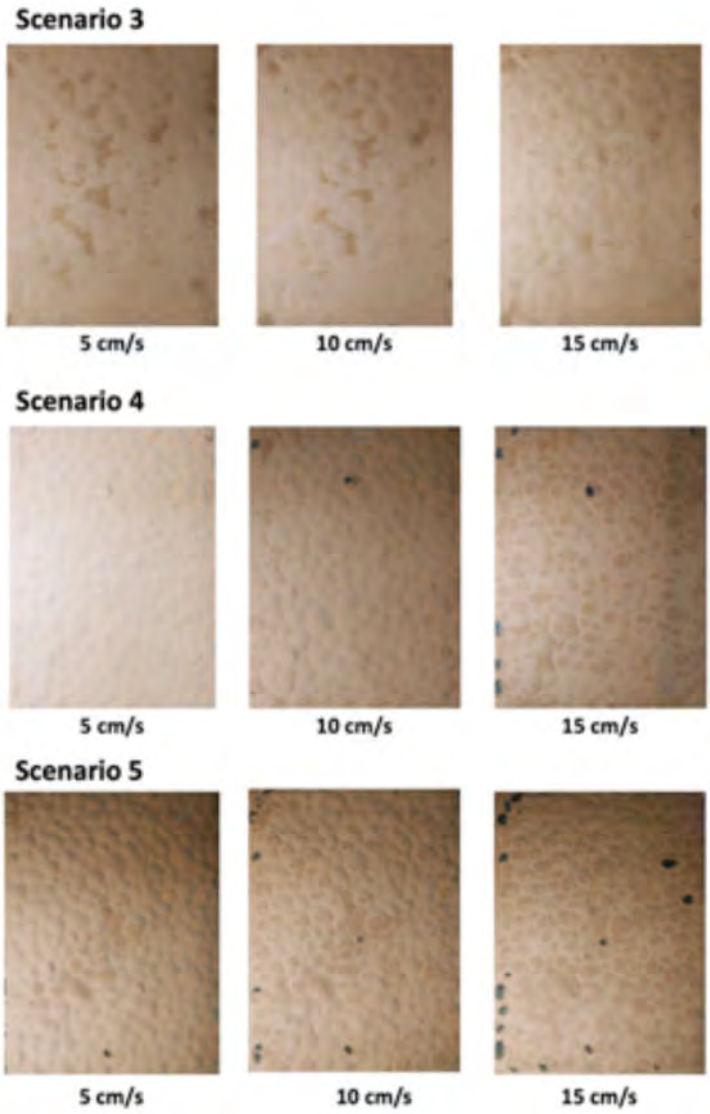

Fig. 18. Resuspension behavior of blanketing layer under increasing flow conditions and different blanketing heights Sc.3: 1 g/L, Sc.4: 0.5 g/L, Sc.5: 0.25 g/L to simulate conditions in a 1 m water column.

G. Flow field analysis of Type 1 nodules

The flow field model from Type 1 nodules under typical deep-sea flow conditions of 0.1 G (4 cm/s) was generated from 13,500 measuring points made with an ADV Vectrino sensor mounted on a 3D Isel arm. The same measuring grid was applied before and after the blanketing experiment for reliable comparison. The overall presentation of the flow field (Z component), including topography, is showed in Fig. 19.

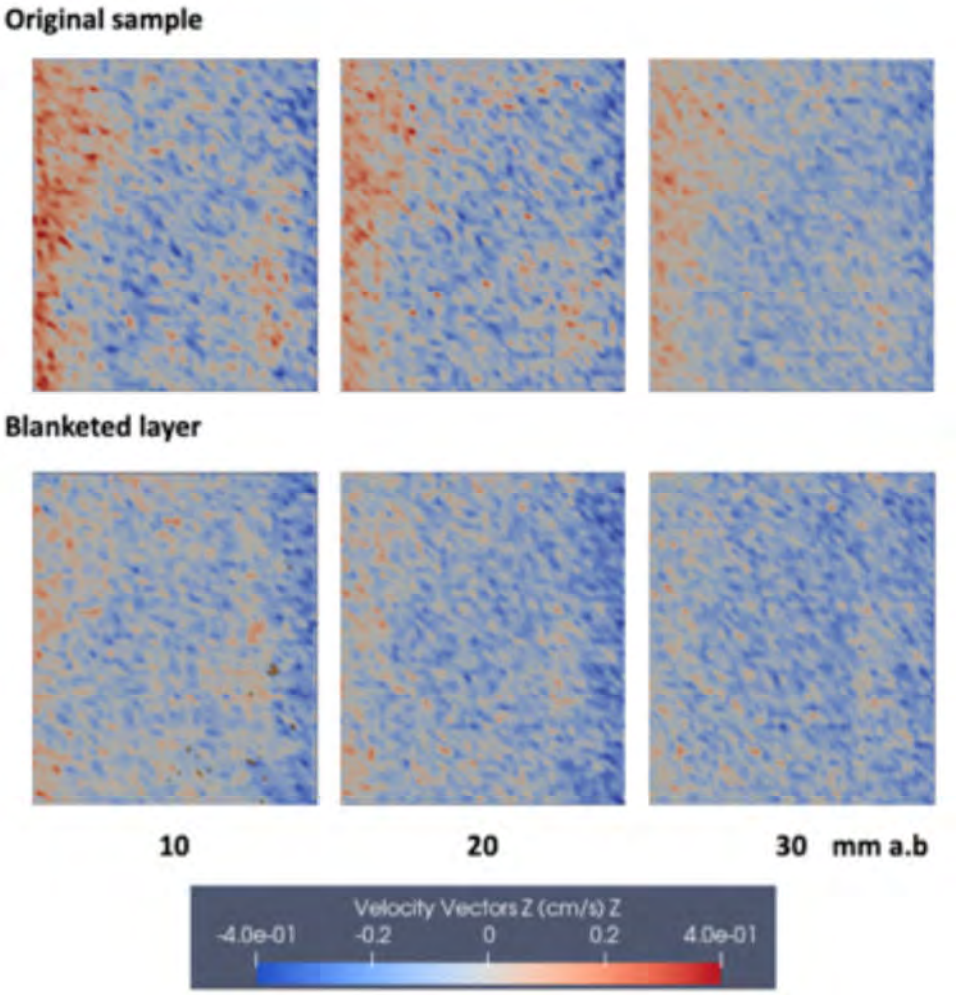

Fig. 19. Flow field comparison in Z direction of the Type 1 nodule test-bed. Flow direction: from left to right

For the original sample, a current deflection in the Z component (up to 0.4 cm/s upward) at the upstream (left) section of the model could be observed. This deflection develops, when deep sea currents enter a Type 1 nodule field and are deviated at the "leading edge" by the new micro-topography. The model also highlights the presence of abundant downward convergence cells (-0.1 to -0.4 cm/s; blue color), which are always associated with upward movement. From an ecological point of view, those observations are crucial. The turbulence is needed for benthic interface feeders to access food which would normally pass by. The turbulence above Type 1 nodules however is significantly lower than above Type 2 or 3 nodules.

After the blanketing, not only the topography had drastically changed (Fig.19, blanketed layer), but the convergence cells close to the seafloor have almost disappeared (Fig. 20B).

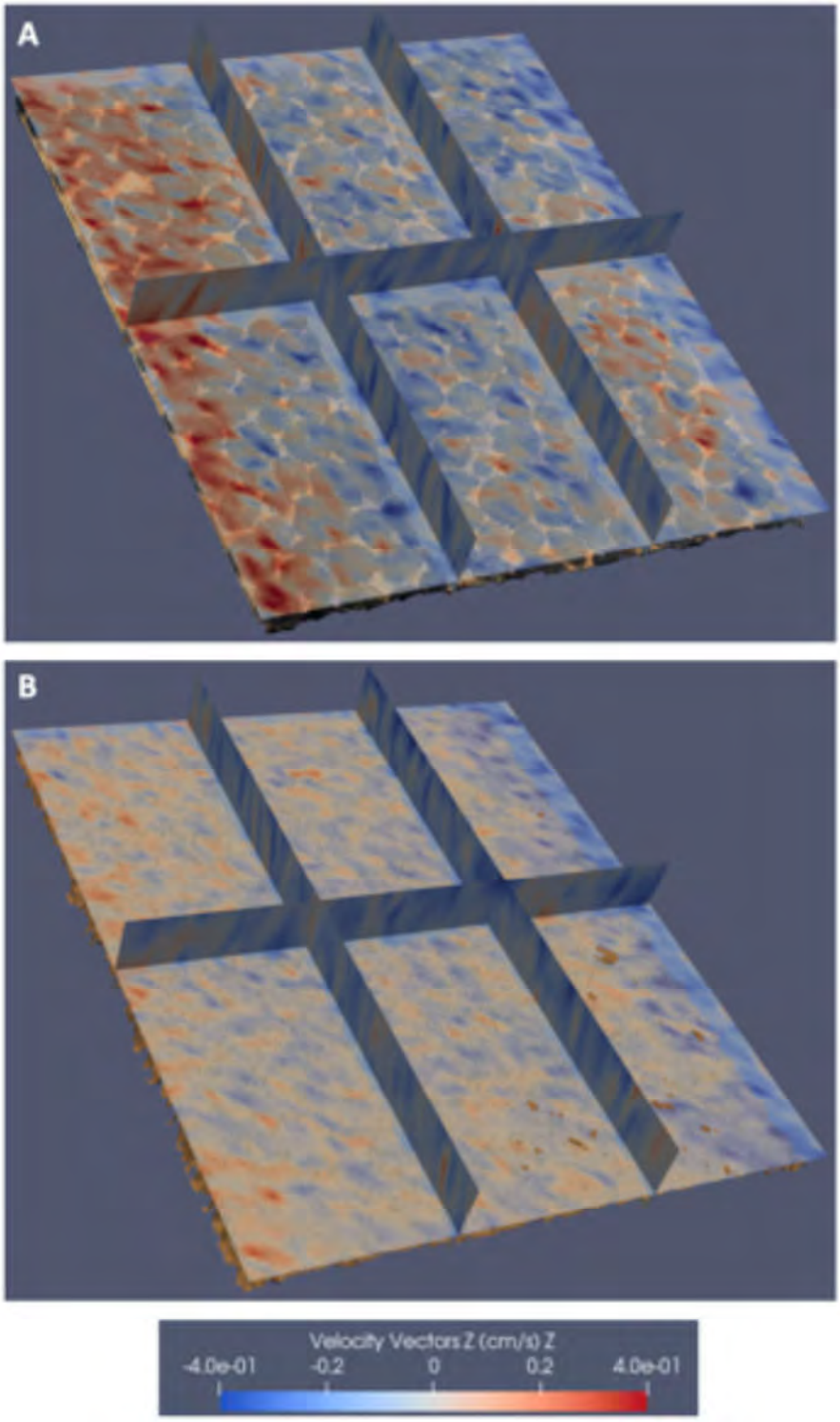

Fig. 20. Flow field measurement of Type 1 nodules. A: Original sample; B: After blanketing; Flow from left to right

Brief evaluation of the results for ecosystem functioning (L.Thomsen)

From an ecological point of view, decreasing water exchange within the BBL and increasing flow magnitude will impact the benthic communities. Benthic filter feeders, which have survived the blanketing episode, might therefore experience an organic matter depletion from the upper water column. This however will mainly take place in areas with Type 2 and 3 nodules where the change from original sediment surface to blanketed surface is much more pronounced, when a full blanketing took place. Small nodules create lower turbulence levels within the last centimeters above seafloor. The GIS map on nodule abundances in the NORI D site shows areas of ridges, troughs as well as flat landscapes. The geomorphology should have an influence on ecosystem functioning. Rougher terrain is more prominent in the Northern part of the Nori site. In trough landscapes megafauna showed the greatest variations in other studies. While regional CCZ benthic ecology has been suggested to be controlled by a gradient of POC flux to the seafloor local environmental factors presumably regulated by geomorphology, such as bottom water flows, nodule occurrence and xenophyophore test density may be important at the local scale. (Simon-Lledó et al. 2019).

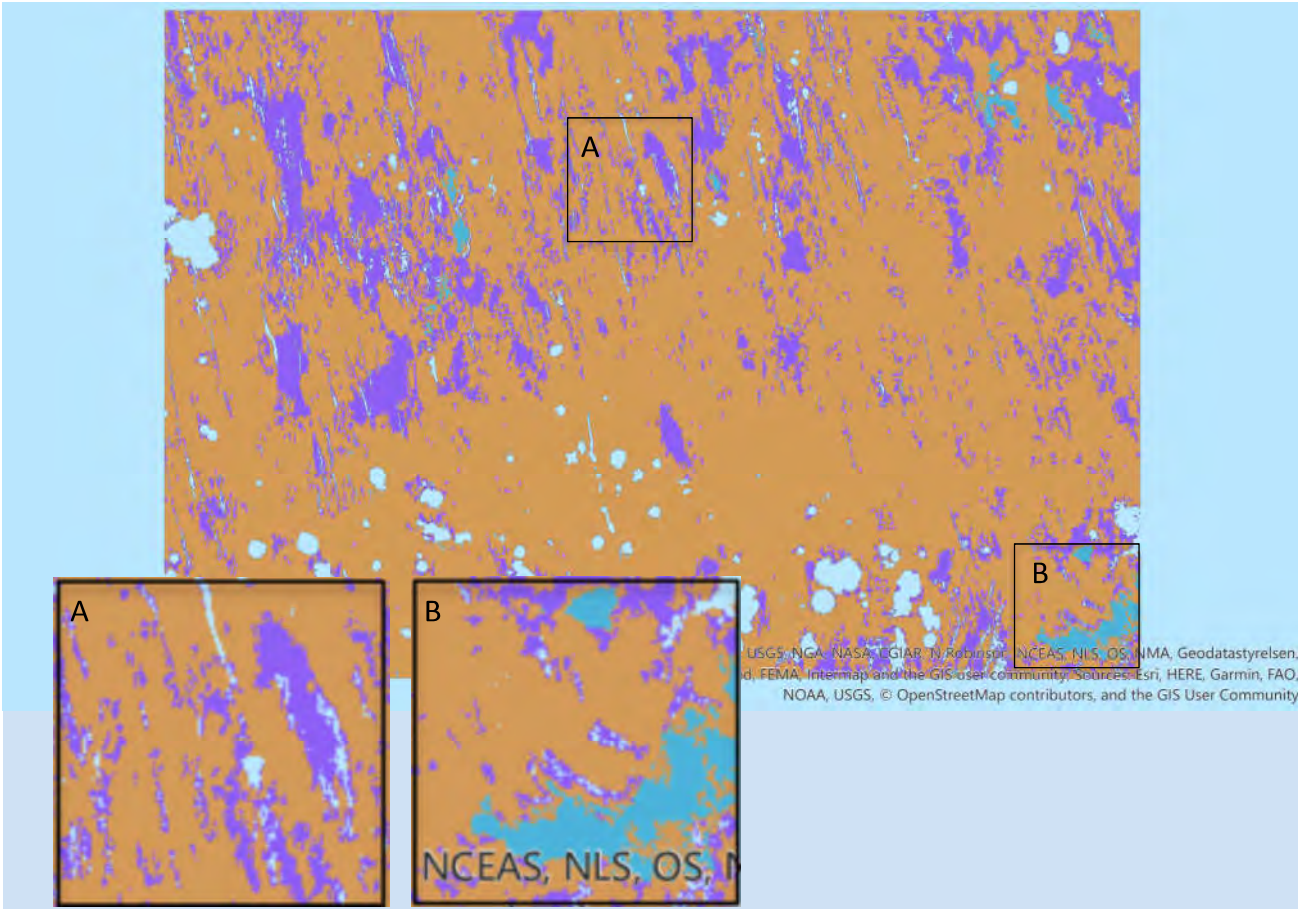

Fig. 21. GIS Map of NORI site, no scaling was provided. (approx. > 10 000 km^2)
Brown: Type 1 nodules
Purple: Type 2, 3 nodules
Light blue: Ridges and seamounts, rocky surfaces (strong backscatter)
Dark blue: valleys without nodules (M.Clarke per. Communication) or flat areas without nodules.

Low sedimentation rates or even a sedimentation interruption and the formation of an erosional surface may have provided suitable conditions for the formation of a great number of small particles which have acted as nuclei to start the growth of nodules. The larger hydrogenetic fraction of small-sized nodules indicates that they have generally formed under lower sedimentation rates compared to the larger nodules (Kuhn et al., 2020).

The importance of nodule abundance on megafaua and macrofauna

The following section discusses the current knowledge and some hypotheses. For the public perception the visible megafauna (> 2 cm in size) is important and shows the fragility and need for protection. For authorities as well as many scientists, macrofauna and megafauna are in focus of conservation initiatives (Danovaro,...Levin, ...Thomsen et al., 2020). To the best of the knowledge of the authors, there is no single ongoing, nor planned, monitoring strategy of a national agency based upon or prioritizing microbial or meiofaunal diversity in their standard protocols.

Macrofauna density **appeared** to increase with increasing nodule abundance in the seabed but to my knowledge, there is no study which **quantifies nodule size** with megafuaunal abundance and diversity. In my opinion, **megafauna** needs larger nodules as solid hard substrate for suspension feeding. The drag of even low deep sea currents would capsize a small nodule.

Fig. 22. (credit: Diva Amon and Craig Smith, Uni Hawaii)

Fig. 23. Small octopus wrapped itself around its eggs on the stabile stalk of a dead deep-sea sponge which was either attached to a larger nodule or deep within the sediment to avoid toppling.
(credit: Autun Purser, AWI OFOS team)

The hypothesis that larger nodules provide better substrate for megafauna is supported for example by a study on glacial dropstones enhancing seafloor species richness of benthic megafauna. These dropstones can be seen as example for the importance of larger nodules and as a suggestion how to restore biodiversity with larger hard substrate (stones). The study revealed a positive correlation between dropstone size and species richness, as well as an increase in the proportion of colonized dropstones with increasing dropstone size (Ziegler et al., 2017).

Personal communication with other experts on megafauna working in the CCZ in other joined projects further supported the idea that nodule size relates to megafauna abundance while high numbers of small nodule do not.

Current knowledge

The following summary presents short text passages from a workshop and a book chapter to present the current knowledge and assumptions:

Smith, C. R., et al. "Deep CCZ Biodiversity Synthesis Workshop Report." *International Seabed Authority (ISA). Friday Harbor, Washington* (2019)
And from the book chapter:
Kuhn, Thomas, et al. "Manganese nodule fields from the Northeast Pacific as benthic habitats." *Seafloor Geomorphology as Benthic Habitat*. Elsevier, 2020. 933-947.

• Megafauna play a significant role in deep-sea ecosystem function, in terms of phytodetritus consumption and bioturbation and carbon flow through the abyssal Pacific food web. Megafaunal density and morphotype richness were investigated in relation to modeled nodule abundance and POC flux to the

seafloor **but the biological data were of insufficient ranges for statistically robust trends to be drawn in some cases** (Kuhn et al., 2020)

• About 50% of all megafauna were shown to depend on nodules (Amon et al. 2016). While higher numerical densities have been observed in locations with higher nodule coverage of different sizes (Vanreusel et al., 2016), **the precise role of nodules and other local environmental factors in the ecology of CCZ megafauna is still poorly understood and based on relatively small areas sampled** (Simon-Lledó et al. 2019). Vanreusel et al. (2016) however, compared the area APEI3 with the BGR site North of NORI and concluded that POC flux is controlling Macro- and Megaufaunal abundances and not nodule abundance.

• Macrofauna is dominated by polychaets. The model explaining the most variance in mean polychaete abundance (numerical density) included POC flux and nodule abundance. The influence of POC flux was highly statistically significant **but the influence of nodule abundance was not**. Interestingly polychaete abundance seems rather negatively correlated with nodule abundance in some areas. Nodule abundance and depth, when assessed individually with Type II regression, exhibited weaker negative exponential relationships with polychaete abundance (Smith et al., p.85 of workshop report)

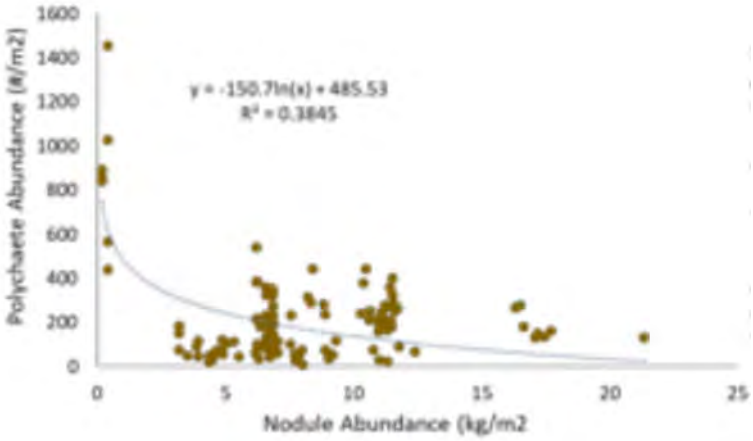

Fig. 24. Polychaet abundance versus nodules abundance (Smith et al., p.85 of workshop report)

Evironmental control and Ecosystem functions

Organic carbon input is considered as key variable for ecosystem functioning in the deep sea and SCOC (sediment community oxygen consumption) is an important parameter to analyze it (Danovaro et al., 2020), preferably on temporal and special scale.

• Multiple regression analysis on SCOC rates measured across the central Pacific revealed that POC flux was the only significant factor (p=0.006) affecting benthic respiration rather than nodule abundance for areas with little nodule abundance (< 10 kg/ m^{-2}). Therefore, relationships across a range of nodule coverage were

not possible to assess. **The authors cannot exclude the possibility that nodules may modify SCOC rates through their effect on bottom water current flow and particle and organic C deposition dynamics.** Temporal variability of SCOC and other ecosystem functions are needed; most studies encompass measurements made over hours to days. (Sweetman at al.,in Workshop report).

See also this iSeaMC report on flow fields around small nodules (Fig.20), and Simon-Lledó et al. (2019) on geomorphology.

• The highest densities, species richness and diversity were recorded in the Eastern part of the CCFZ (BGR license area), while the lowest values were found in the APEI3 area, which is rich in nodules but low in POC flux. The results correspond to the differences in productivity observed in the CCFZ (Błażewicz et al., 2019).

• Morphotype richness appeared to slightly increase with increasing nodule abundance but this relationship was weak and not statistically significant (r_S = 0.47, p > 0.05) (Jones et al., p 107 of workshop report). While higher numerical densities have been observed in locations with higher nodule coverage (Vanreusel et al., 2016), the precise role of nodules and other local environmental factors in the ecology of CCZ megafauna is still poorly understood and based on relatively small areas sampled (Simon-Lledó et al. 2019)

Nodule cover has previously been shown to be an important factor in the structuring of megafaunal communities (Simon-Lledó et al. 2019), as some taxa are known to require nodule habitat (Vanreusel et al. 2016, Amon et al 2016). However, these patterns are not necessarily linear. Simon-Lledó et al (2019) showed how local megafaunal densities increased describing a rapid asymptote (i.e. stabilising in mid-low nodule abundance levels) over a gradient of nodule coverage. This study also showed that local taxa richness appeared to be invariable across the nodule gradient unless this metric was calculated upon fixed-areal sampling units, as this effectively incorporated faunal density as a factor in the calculation of taxa richness.

Conclusion on nodule size and megafauna

I suggest that DG analyses many video transects from the Type 1 nodule sites to verify or falsify this hypothesis, combined with SCOC data in enhanced spatial and temporal resolution to quantify the flux of POC. Comparisons based on directly measured nodule abundance from seabed photographs to megafaunal density, also at regional scale, may be best suited to explore such patterns and will help DG to prepare for discussions with the public and authorities.

Comparison with other areas of the CCFZ

Median particle size in these top 15 cm of sediments was in the same range as those from other sites at the CCFZ (d_{50} of 8 to 25 µm respectively). The rapid aggregation within the first 30-60 minutes as well as the development of d_{50} of aggregates was also similar at other sampling sites. At all sites the export phase which resulted in a > 90 % deposition lasted between 60 and 120 m after the stop of release of the plume. Smaller

initial plume concentrations resulted in slower fallout times. This is consistent with results from experiments on concentrations < 500 mg with sediments further North of the NORI site. Compared to sites with higher d_{50} of the primary particles (eg 20 µm), the resulting settling velocities of the aggregates at the NORI D site were higher, most probably the result of denser packed aggregates of smaller original particles. Blanketing layer thickness at other locations under 0.5 and 1 g/L scenarios were in the same range.

Concluding remarks

Close collaboration with AllSeas should clarify the expected range of particle concentrations -and size at the midwater injection point and behind the collector. Then modeling of plumes will give best estimates of the impact areas.

Following the suggestions of Mingotti and Woods (2020) the plume would create a water layer of enhanced particle concentration where turbulent aggregation will result in rapid vertical export; or turbulent dispersal is so strong that aggregation is prevented and fine particles are diffusing into the deep Pacific as suggested by others. Results from Dredging should give insights into that process. For deep sea mining activities, there is only one short video sequence from MIT available, which indicates particle fallout. In accordance with Mingotti and Woods (2020) we assume that the flow is turbulent which support aggregation and the particles and fluid descend to the level at which the bulk speed of the flow falls to zero. After an initial overshoot, the flow begins to spread laterally at its neutral buoyancy level. There is then a zone of fluid–particle separation, with particles falling down while the residual fluid becomes more buoyant (see Fg. 4, Mingotti and Woods, 2020). We assume midwater concentrations of ≈ 10 g/L now and nodule fines which might modify aggregation.

Same holds true for the exhaust pipe behind the collector. The plume will descent down to the seafloor and aggregation will take place. Data with real expected concentrations should be used for experiments. We assume concentrations of > 40 g/L now. The fluid mud layer will rapidly produce hindered settling or even gelling. An injection of nodule fines might change the transport behavior of these highly concentrated fluid muds before. Only those data will provide best prerequisites for reliable prognosis, before a collector test will give real answers to these important questions.

iSeaMC can discuss the results of this report with the DG Modelers to decide on the best suited particle characteristics for the current midwater and seafloor injection points.

Additional figures

Fig. S1. Incoming gravity flow under 0.1 G conditions in the seawater flume

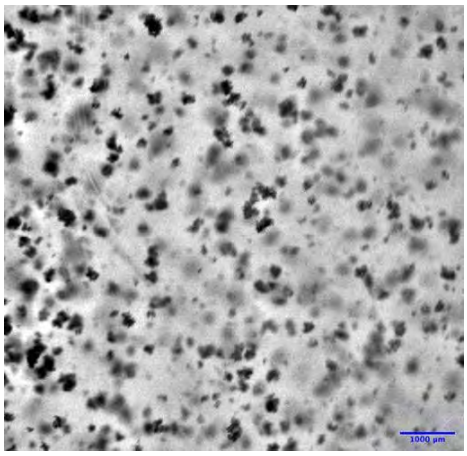

Fig. S2. Suspended aggregates during aggregation of 1 g/L sediment plume at 60 min

Fig. S3 Test vials for fig. 15. Aggregated plume particles were inserted to determine the height of the resulting mud layer

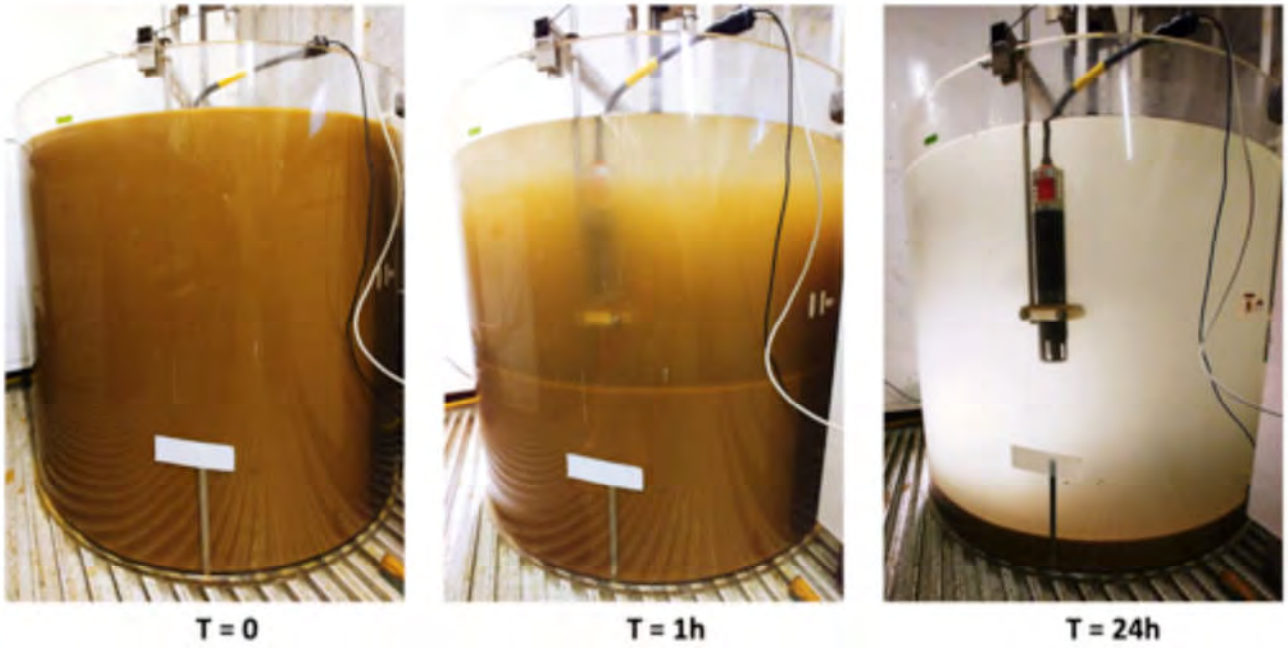

Fig. S4. Development of the fluid mud layer. T0 under 10 g/l, T1 during the export phase of newly formed aggregates which form a unconsolidated mud layer, T24: 1 day after plume release and 22 h after the export phase ended, when the mud layer is consolidated and remaining fine particles < 100 µm will create a new sediment surface.

Fig. S5. Plume aggregates during deposition (0.6 mm: compaction area ; 6 - > 40 mm: agglomeration) in the flume

G. References:

Ahrens, James, Geveci, Berk, Law, Charles, ParaView: An End-User Tool for Large Data Visualization, Visualization Handbook, Elsevier, 2005, ISBN-13: 978-0123875822

Amon, D.J., Ziegler, A.F., Dahlgren, T.G., Glover, A.G., Goineau, A., Gooday, A.J., et al., 2016. Insights into the abundance and diversity of abyssal megafauna in a polymetallic-nodule region in the eastern Clarion- Clipperton Zone. Sci. Rep. 6, 30492.

Błażewicz, Magdalena, et al. "High species richness and unique composition of the tanaidacean communities associated with five areas in the Pacific polymetallic nodule fields." Progress in Oceanography 176 (2019): 102141.

Dankers, P. J. T., and J. C. Winterwerp. "Hindered settling of mud flocs: theory and validation." Continental shelf research27.14 (2007): 1893-1907.

Danovaro, R., Fanelli, E., Aguzzi, J., Billett, D., Carugati, L., Corinaldesi, C., ...Levin, L.,..Thomsen, L., . & McClain, C. (2020). Ecological variables for developing a global deep-ocean monitoring and conservation strategy. Nature Ecology & Evolution, 4(2), 181-192.

Garcia, R., and L. Thomsen. "Bioavailable organic matter in surface sediments of the Nazaré canyon and adjacent slope (Western Iberian Margin)." Journal of Marine Systems 74.1-2 (2008): 44-59.

Gardner, Wilford D., Mary Jo Richardson, and Alexey V. Mishonov. "Global assessment of benthic nepheloid layers and linkage with upper ocean dynamics." *Earth and Planetary Science Letters* 482 (2018): 126-134.

Gillard, B. , Purkiani, K. , Chatzievangelou, D. , Vink, A. , Iversen, M. and Thomsen, L. (2019): Physical and hydrodynamic properties of deep sea mining-generated, abyssal sediment plumes in the Clarion Clipperton Fracture Zone (eastern-central Pacific) , Elementa, 7 (1) . doi: 10.1525/elementa.34

Hill, P.S., Nowell, A.R.M., 1990. The potential role of large, fast sinking particles in clearing nepheloid layers. Philosophical Transactions of the Royal Society of London Series A 331, 103}117.

Hill. P.S. Newgard. J.P.. Law. B.A.. Milligan. T.G.. (2013). Flocculation on a Muddy Intertidal Flat in Willapa Bay. Washington. Part II: Observations of Suspended Particle Size in a Secondary Channel and Adjacent Flat. Continental Shelf Research.

Jackson, G. A. (2015). Coagulation in a rotating cylinder. Limnology and Oceanography: Methods, 13(4), 194-201.

Kuhn, Thomas, et al. "Manganese nodule fields from the Northeast Pacific as benthic habitats." Seafloor Geomorphology as Benthic Habitat. Elsevier, 2020. 933-947.

Mikkelsen. O.. P. S. Hill. T. Milligan. and R. Chant (2005). In situ particle size distributions and volume concentrations from a LISST-100 laser particle sizer and a digital floc camera. Cont. Shelf Res.. 25. 1959–1978.

Mingotti, Nicola, and Andrew W. Woods. "Stokes settling and particle-laden plumes: implications for deep-sea mining and volcanic eruption plumes." Philosophical Transactions of the Royal Society A 378.2179 (2020): 20190532.

R. G. A. Craig, C. Loadman, B. Clement, P. J. Rusello and E. Siegel, "Characterization and testing of a new bistatic profiling acoustic Doppler velocimeter: The Vectrino-II," 2011 IEEE/OES 10th Current, Waves and Turbulence Measurements (CWTM), Monterey, CA, 2011, pp. 246-252. doi: 10.1109/CWTM.2011.5759559

Sanford LP (1997) Turbulent mixing in experimental ecosystem studies. Mar Ecol Prog Ser 161:265–293

Simon-Lledó, E., Bett, B.J., Huvenne, V.A., Schoening, T., Benoist, N.M., Jeffreys, R.M., Durden, J.M. and Jones, D.O., 2019. Megafaunal variation in the abyssal landscape of the Clarion Clipperton Zone. Progress in oceanography, 170, pp.119-133.

Smith, C. R., et al. "Deep CCZ Biodiversity Synthesis Workshop Report." International Seabed Authority (ISA). Friday Harbor, Washington (2019)

Stolzenbach, K.T., Elimelech, M., 1994. The e!ect of particle density on collisions between sinking particles: implication for particle aggregation in the ocean. Deep-Sea Research I 41 (3), 469}483.

Thomsen L, McCave IN (2000) Aggregation processes in the benthic boundary layer at the Celtic Sea continental margin. Deep-Sea Research I, 47, 1389-1404.

Thomsen. L.. Gust. G.. 2000. Sediment erosion thresholds and characteristics of resuspended aggregates on the western European continental margin. Deep Sea Research Part I: Oceanographic Research Papers 47. 1881–1897.

Tinevez, JY.; Perry, N. & Schindelin, J. et al. (2017), "TrackMate: An open and extensible platform for single-particle tracking.", Methods 115: 80-90, PMID 27713081

Tran, Duc, Rachel Kuprenas, and Kyle Strom. "How do changes in suspended sediment concentration alone influence the size of mud flocs under steady turbulent shearing?." Continental Shelf Research 158 (2018): 1-14.

Vanreusel, A., Hilario, A., Ribeiro, P. A., Menot, L., & Arbizu, P. M. (2016). Threatened by mining, polymetallic nodules are required to preserve abyssal epifauna. Scientific reports, 6, 26808.

Ziegler, A. F., et al. "Glacial dropstones: islands enhancing seafloor species richness of benthic megafauna in West Antarctic Peninsula fjords." Marine Ecology Progress Series583 (2017): 1-14.

Smith, C. R., et al. "Deep CCZ Biodiversity Synthesis Workshop Report." International Seabed Authority (ISA). Friday Harbor, Washington (2019)

And from the book chapter: